

MODERATE DENSITY REGIONS IN THE LYND 134 CLOUD COMPLEX

R.J. Laureijs^{1,2}, Y. Fukui³, G. Helou¹, A. Mizuno³, K. Imaoka³, F.O. Clark⁴

¹Infrared Processing and Analysis Center, JPL, Caltech
Mail Code 100-22, Pasadena, CA 91125, USA

²Space Science Department, ESTEC
P.O. Box 299, 2200 AG, Noordwijk, The Netherlands

³Radioastronomy Laboratory, Dept. of Astrophysics
Nagoya University, Chikusa-ku, Nagoya 464-01, Japan

⁴Geophysics Directorate - Phillips Laboratory, GPOB
29 Randolph Road, Hanscom Air Force Base, MA 01731-3010, USA

Running Headline: The L134 Cloud Complex
To be published in: The Astrophysical Journal Supplements

Received September '94; accepted February '95

Address for proofs:

R.J. Laureijs
SAI/SSD ESTEC, P.O.B. 299
2200 AG Noordwijk, The Netherlands
Email: rlaureij@isosa6.dnet.estec.esa.nl (internet)

Version: 22 February 1995

Abstract

IRAS images, carbon monoxide observations at 2.7 mm (CO , ^{13}CO , and C^{18}O), and blue extinction from star counts have been used for a large scale study of the 1.134 complex of high latitude clouds. We have correlated the different tracers in order to investigate the range of physical conditions for which these tracers apply. We find tight linear correlations between ^{13}CO and A_B , and ^{13}CO and ΔI_{100} . The quantity ΔI_{100} is the infrared emission of inner cloud regions obtained from the relationship $\Delta I_{100} = I_{100} - I_{60}/\Theta$, where Θ is the value for I_{60}/I_{100} in the outer regions of the clouds. We find that ΔI_{100} probes the same regions as ^{13}CO and can therefore be used to predict the ^{13}CO emission. From the correlation between ^{13}CO and A_B , and the CO measurements we determine an average ^{13}CO abundance in the complex which does not differ significantly from other studies. However, the abundance in the translucent cloud L1780 is about a factor 4 lower than in the opaque clouds 1.134, L183, and L169.

Using the ^{13}CO observations we have compiled the properties of 18 clumps in the complex. The clumps follow clear luminosity-size and size-linewidth relationships. The size-linewidth relationship is consistent with a power law with exponent 0.5. The derived ambient pressure acting on the clumps is of order $p/k = 2 \times 10^4 \text{ K cm}^{-3}$.

Both molecular and infrared data show that the ultraviolet radiation field in the complex is anisotropic. This is consistent with the presence of the nearby UV sources $\zeta \text{ Oph}$ and the Upper Scorpius OB association. The densest regions in the complex as delineated by the ammonia cores can be found close to the low illumination edges of the clouds. In addition, a higher density contrast on the shadow side can be observed. These observations support the view that the anisotropic UV field affects the density distribution in the clouds and that the increased strength of the UV field causes a bigger halo on the illuminated side. The influence of the UV field upon the appearance of clouds is most evident in the outer layers of a cloud. The inner, denser, and well-shielded parts seem much more similar. Judging by the uniform behaviour of most tracers. However, the displacement of the ammonia cores with respect to the cloud centers suggests the effects of the anisotropy extend down to the densest layers of the clouds.

Subject headings: infrared emission, molecules, molecular clouds

1. Introduction

The structure and interior physics of interstellar clouds are often inferred from molecular line observations. The interpretation of molecular lines, however, depends upon parameters (such as fractional abundance, excitation degree, and line saturation degree) that are difficult to determine independently. An alternative tracer is infrared emission from dust. IRAS has provided an all-sky database to study infrared emission at 12, 25, 60 and 100 μm . With the development of improved mapping algorithms, structures can be studied with an accuracy better than previously possible using the same initial data. This allows detailed analysis of molecular clouds including the smaller and cooler ones with relatively low surface brightness.

The interpretation of diffuse IRAS emission is not straightforward due to the presence of different dust components. The 10 – 100 μm emission has been attributed to a panicle mix which consists of large molecules, very small grains, and classical grains (Draine & Anderson 1985; Chlewicki & Laureijs 1988; Mathis & Whiffen 1989; Helou, 1989; Désert, Boulanger & Puget 1990). Boulanger et al. (1990) added a new dimension to the complexity by observing infrared color variations which cannot be explained by models assuming a fixed grain composition. These variations may reflect changes in dust composition.

In this paper, we combine data on dust and molecular line emission. We analyze the morphology and properties as well as the interrelationships between frequently used tracers of molecular clouds: carbon monoxide emission at 2.7 mm, infrared emission detected by IRAS, and blue extinction derived from star counts. Special attention is given to the presence of strong infrared color variations and molecular line emission as reported by Boulanger et al. (1990), Laureijs, Clark & Prusti (1991), and Abergel et al. (1993).

The complex of clouds centered around the dark cloud L134 (Lynds 1962) is a suitable region to analyze diffuse and dense parts in clouds. The complex is situated at high galactic latitude ($l=5^\circ, b=36^\circ$) which minimizes the likelihood of unrelated emission along the line of sight. A distance to the complex of 11.0 ± 1.0 pc was measured by Franco (1989) from photometric observations of field stars. The proximity to the sun allows study of small linear scales even with the limited IRAS resolution of about $5'$ which corresponds to 0.16 pc. The clouds L134 and L183 contain dense cores which have been studied extensively in the past (e.g. Mattila 1979; Clark and Johnson 1981, Swade 1989a, 1989b and references therein). In addition, the complex includes a number of lower opacity molecular clouds previously detected in CO (Magnani, Blitz & Mundy 1983). In Table 1 we have listed the names and positions of the main clouds we investigate in this study.

The observational procedures and data collection are described in section 2. Carbon monoxide and infrared images are presented in section 3. This section includes a description of the position of the L134 complex in its galactic neighborhood. In section 4.2-4.5 we analyze mostly empirically general correlations between infrared, carbon monoxide, and extinction in the four densest clouds. In section 4.6 the influence of the anisotropy of the UV radiation field is examined by considering slices through two clouds. The properties of ^{13}CO clumps are investigated in section 4.7. In section 5 we interpret the measured quantities and correlations by comparison with previous observations and models. In section 6 we discuss our observations in terms of cloud stability and structure. We present evidence that the anisotropic radiation field in the complex affects the morphology of the clouds. The conclusions are stated in section 7.

2. Observational Material

2.1. Carbon Monoxide

Spectral lines of the CO, ^{13}CO , and $\text{C}^{18}\text{O } J=1-0$ transitions were collected with the 4 meter telescope of the University of Nagoya (Kawabata et al. 1985) in the period December 10, 1990- January 14, 1991. The telescope has a spatial resolution of 2.7 (FWHM) and is equipped with a Helium cooled SIS receiver (Ogawa et al. 1990). Spectra were obtained by switching the frequency over an interval of 13 MHz. To ensure that we did not overlook broad spectral features, deep position-switched spectra were taken at suspect broad-wing positions. The channel separation of the 1000 channel acousto optical spectrometer was 50 kHz, corresponding to a velocity resolution of 0.13 km s^{-1} at 115 GHz. The system temperature was of order 200-300 K for ^{13}CO and C^{18}O at 110 GHz, and 600-800 K for CO at 115 GHz. The target rms noise per channel was chosen to be less than 0.1, 0.4, and 1.2 K for the C^{18}O , ^{13}CO , and CO lines, respectively. During optimum sky conditions, an integration time of 20 seconds was sufficient to obtain an rms noise level of less than 0.35 K per channel at 110 GHz.

Both stability of the receiver and elevation dependencies were monitored by frequent observation of the L183 ammonia core (RA $15^{\text{h}} 51^{\text{m}} 30^{\text{s}}$, Dec $-2^{\circ} 43' 31''$; Ungerechts, Walmsley & Winnewisser 1983; Swade 1989a) and by determination of the atmospheric opacity τ by means of sky-dipping. The peak antenna temperature T_A^* of the reference line varied by less than 5% when the elevation angle z varied between 30° and 50° . Since this variation is of order the relative uncertainties in the peak temperatures (3-10%), we ignored the systematic variations within the observed elevation range. Extrapolation of the empirical linear relationship between T_A^* and $\tau \csc(z)$ to $z=90^{\circ}$ showed that the spectral lines would be on average 5% and 10% brighter at 110 and 115 GHz, respectively, when observed in the zenith. Accordingly, correction factors of 1.05 and 1.10 have been applied.

The absolute temperature calibration was performed by daily observation of the Orion-KL position. The average peak T_A^* was observed to be 65 K by fitting a gaussian line profile. This result has been compared with $T_{\text{MB}}=84 \text{ K}$, the brightness temperature measured with the Millimeter Wave Observatory of the University of Texas (Schloerb and Loren, 1988; Wootton, private communication). Assuming that the beam of the 5 meter MWO telescope is similar to that of the Nagoya telescope, a forward spillover correction of $\eta_{\text{FSS}}=65/84=0.8$ was adopted to convert T_A^* to T_{R}^* (Kutner and Ulich 1979).

Similar observations of the Orion KL position in the other CO isotopes yield values for η_{FSS} that are 10-25% lower than the value found for CO (namely 0.7 and 0.6 for ^{13}CO and C^{18}O , respectively), depending upon the adopted reference T_{R}^* . We have not corrected the data for these results but rather considered the different η_{FSS} as part of the uncertainties in the calibration of the carbon monoxide data. Consequently, we estimate an uncertainty in the temperature calibration of at most 25%.

The frequency switched spectra were corrected for baseline ripples and zero level offsets by subtracting third order polynomial fits. In the following sections we denote the velocity integrated emission $\int T_{\text{R}}^* dv$ of CO, ^{13}CO , and C^{18}O by W_{12} , W_{13} , and W_{18} , respectively. For comparison with the infrared and extinction maps, the CO maps have been convolved with a Gaussian to an effective resolution of 5.4 arcminutes.

2.2. Infrared

IRAS images at 12, 25, 60, and 100 μm were obtained using BIGMAP 2 coadding software (Wheelock and Kester 1989). Before coaddition, the individual scans at 12, 25 and 60 μm were smoothed to a spatial resolution of $5'$ to match the resolution at 100 μm . The zodiacal emission was removed from the scans by subtraction of the semi-empirical model derived by Good (1988). We note that one of the zodiacal γ -bands runs parallel to the Ecliptic plane approximately through RA $= 161^{\text{h}} 00^{\text{m}}$, Dec $= -6^{\circ} 00'$. The band runs just below the central cloud complex but above 1,1780. Since the band has a colder spectral distribution (than the zodiacal dust cloud we do not expect any serious contamination in the main clouds by the γ -band

at 12 μm . At 100 μm the excess emission is negligible. At 2.5 and 60 μm there may be an additional gradient. In order to extract the emission associated with the clouds only, we applied an additional background subtraction by removing a tilted plane that has been fitted to emission free regions of the images. These regions were determined by eye.

We also used the All-Sky IRAS low resolution maps with 0.5×0.5 pixels for which the zodiacal emission was subtracted using the Good (1988) model (Oken, Gautier & Wheelock 1988).

2.2. Extinction

A blue extinction (A_B) image derived from star counts of an ESO J plate has been taken from Mattila and Schnur (1994). The initial star count map has a reseau size (and pixel size) of 5.6×5.6 and covers an area of about 2.5×2.5 centered at RA = $15^{\text{h}} 51^{\text{m}}$, Dec = $-3^\circ 0'$. The extinction map includes L183, L169, and a large fraction of L134. Star count data of 1,1780 with $3' \times 3'$ resolution have been taken from Mattila (1979). The star counts of L1780 were converted to extinction using the method described in Mattila (1986) and subsequently smoothed to a resolution of $5'$.

3. Presentation of the data

3.1. Infrared Morphology

To show the location of the L134 complex in the infrared sky, we have displayed 100 μm images on two different scales in Fig. 1. The large scale image (Fig. 1a) shows that the L134 complex is on the edge of an extended infrared emission region with the Ophiuchus complex of dark clouds approximately in its center. This region runs from galactic longitude $l=330^\circ$ to $l=25^\circ$ and extends out to about $b=40^\circ$ at $l=0^\circ$. Studies of the Ophiuchus complex of dark clouds (de Geus 1990, and references therein) and the Upper Scorpius OB association (Blaauw, 1991) have indicated that the region must be shaped by supernova explosions and stellar winds from the OB association. Another molecular study by Nozawa et al. (1991) has shown that the star formation rate is remarkably low in the northern part of the Ophiuchus complex, and has suggested that the strong UV radiation may play a role in regulating the rate through enhancing the ionization rate of the molecular gas. The elongated structure in which the L134 complex is embedded appears in Fig. 1 as one of the most distant filaments surrounding the Upper Scorpius OB association. The filament can also be seen in the HI maps presented by Colomb, Poppel & Heiles (1980). On a smaller scale, (Fig. 1 b) the filament consists of fragments in which the dark clouds L183 and L134 are the brightest features. The dense clouds, including the smaller clouds MBM38 and MBM39 are situated on the edge of a bubblelike structure of about 5° in diameter centered on $l=8^\circ, b=40^\circ$. L183 and L134 are elongated in the direction perpendicular to the filament.

Photometric measurements of late type stars by Franco (1989) show that the L134 complex is embedded in a region of size of about $8^\circ \times 50'$, with a photometric distance of 11.0 ± 1.0 pc, and a color excess of $E(b-y)=0.2$ mag. The large extent of the region suggests that Franco measured the distance to the filament seen in emission at 100 μm . Franco's distance determination compares well with the distance of 160 pc determined by Snell (1981), who applied the same method but used brighter stars in a $20^\circ \times 200'$ area obtained from published catalogs. As Franco surveyed a smaller area of $8^\circ \times 90'$, the larger region that has been analyzed by Snell could be biased by clouds in the related Ophiuchus cloud complex. This is consistent with the upper limit of 170 pc for the distance to the Ophiuchus cloud complex as estimated by de Geus et al. (1990). We also conclude that the L134 complex and the Ophiuchus complex are related as suggested by the infrared morphology.

The dark clouds are readily distinguished as areas of brighter 100 μm emission (Fig. 1 b). The clouds 1.183, 1.134, and 1.169 are connected by low brightness filamentary structures. The association of MBM 39 and MBM 38 with the main complex is suggested by the connecting cirrus regions. L1780 appears isolated from the emission region around LJ 34 and 1.183, and is situated in an empty region between two larger structures. The lack of surrounding material has also been noticed by Franco (1989) from the analysis of the color excess of stars. L1780 exhibits a cometary tail pointing in the direction of Upper Scorpius OB association. We note that the clouds 1.1778 and 'feature 2' measured by Clark and Johnson (1981) correspond 101,1780 and 1.169, respectively, in this study.

The center of the 1.134 complex in the four IKAS bands is presented in Fig. 2. In the immediate vicinity of the dark clouds 1.183 and LJ 34, we observe a poor correlation between the emission at 12 and 25 μm on the one hand and 100 μm on the other. Both the 12 and 25 μm images show a gradual increase in brightness from North to South. The position of the center of 1.134 is associated with a well defined emission minimum encircled by a rim of 12 μm emission. We see no emission at 12, 25 and 60 μm that can be related to the northern region of 1.183 where the ammonia core resides. Most noticeable at 25 μm is the rim on the SE side of 1.134, with a center just greater than its counterpart of 12 μm . The 60 μm image shows a good correlation with the 100 μm morphology, but the correspondence breaks down in the higher opacity regions.

The infrared maps of the other clouds are displayed in Figs. 3 (L1780), 4 (MBM 39), and 5 (MBM 38). MBM 39 lies on the edge of an extended emission region with a North-South gradient. Since MBM 38 exhibits no detectable 12 and 2.5 μm emission above the noise level, we have left out its images at these wavelengths.

We have found no infrared point sources in the images as well as in the IRAS point source catalog that could indicate the presence of a potential young stellar object related to the clouds. Strong infrared point sources in the complex are either COO stars with a rising spectrum towards shorter wavelengths, or galaxies peaking at 60 μm .

3.2. Carbon monoxide survey

The morphology of CO and ^{13}CO emission in the inner area of the LJ 34 complex at velocity intervals of 0.4 km/s as well as the contour maps of total integrated emission are presented in Fig. 6, 7, and 8. The positions of the ammonia cores in L134 and 1.183 (Myers and Benson, 1983) have been marked on the maps.

The carbon monoxide morphology shows some differences with the 100 μm images. At 100 μm , the emission associated with L183 appears to be elongated in the N-S direction whereas the CO emission of the same region is concentrated along a bar or filament that runs in the E-W direction. At position RA=15^h53^m20^s, Dec=-2°35' in the velocity interval $v=0.6-1.8$ km/s, CO emission has been detected that has no obvious counterparts in the infrared and in ^{13}CO . Several CO cloud components (or clumps) can be discerned at different velocities in the 1.134 complex. Both the elongated feature associated with L183 as well as L134 exhibit a number of local emission peaks.

The position of the ammonia cores in 1.183 and L134 cannot easily be predicted on the basis of the CO or ^{13}CO maps alone. The ^{13}CO emission maxima in both L134 and 1.183 appear to be several arcminutes south of the dense cores. The integrated intensity maps (Fig. 8) suggest that the densest regions in the clouds are not in the center but on the edges of the structures detected in either CO or ^{13}CO . The velocity maps (Figs. 6 and 7) exhibit a systematic velocity variation over the complex: the lower velocity features are situated on the eastern side, and appear to consist of smaller clumps scattered over a

larger area.

The line integrated emission of three isolated ^{13}CO clouds are given in Fig. 9 (L1780), Fig. 10 (MBM 39) and Fig. 11 (MBM 38). L1780 has a regular morphology especially in ^{13}CO where it has only one narrow velocity component ($\Delta V=0.6$ km/s). The other clouds consist of several distinct components. The three smaller clouds clearly show that ^{13}CO peaks at positions different from those detected in CO. In addition, comparison between the ^{13}CO and CO contours shows evidence that the ^{13}CO contours are systematically displaced in the NW direction.

4. Analysis

4.1. Radiation Field

In this section we describe the radiation field in L134 using distance estimates of the cloud complex and nearby O11 associations. We only consider the UV component of the interstellar radiation field (ISRF) as the other emission components are more uniformly distributed on linear scales of a few hundred pc (Habing 1968, Mathis et al. 1983).

Analysis by Blaauw (1991) of the 3 dimensional distribution of the OB associations within 1.5 kpc from the sun indicates that the L134 complex with a z -height of 65 pc is situated above all local associations. Apart from Upper Scorpius, all nearby associations such as Ori-1, Per-2, and Lac-1, are situated below the plane of the Galaxy. In addition, these associations are at least 500 pc away from L134. The study by Blaauw confirms the suggestion by Mattila (1986) that the UV field in L134 comes mainly from one direction.

The nearest dominant UV sources are the Upper Scorpius OB association at a heliocentric distance of $d_0=158$ pc and the O9.5V star ζ Oph at $d_0=228$ pc (de Geus, de Zeeuw & Lub, 1989). The distances indicate that both sources are situated behind the L134 complex (at 110 pc) with separations of 70 pc between L134 and Sco OB2, and 123 pc between L134 and ζ Oph. Using stellar UV parameters of Habing (1968) and assuming no extinction from intervening dust we derive radiation densities of 11, 8, and $210 \cdot 10^{-17}$ erg cm $^{-3}$ Å $^{-1}$ at 1000, 1400, and 2200 Å respectively, in the vicinity of L134. The derived radiation density at 1000 Å is more than 2 times the canonical value for the general interstellar radiation field at 1000 Å as obtained by Mathis et al. (1983; $4.9 \cdot 10^{-17}$ erg cm $^{-3}$ Å $^{-1}$ at 1000 Å).

The visual extinction towards ζ Oph and δ Sco (member of Sco OB2) is 0.9 and 0.5, respectively (de Geus 1990). From these numbers we estimate a visual extinction between the UV sources and the L134 complex of at most 0.5 mag. Depending on the UV grain albedo and the far-UV extinction properties (e.g. Savage & Mathis, 1979), at most 80% of the UV photons will be absorbed if $A_V=0.5$ (Habing 1968).

In conclusion, assuming that dust extinction is negligible between the stars and the L134 complex, we infer that (i) the energy density can be as high as 3 times the average value of $4.9 \cdot 10^{-17}$ erg cm $^{-3}$ Å $^{-1}$ at 1000 Å, if we add the presence of a diffuse UV component and (ii) the UV field at L134 is anisotropic with 2 times more radiation from one direction. This radiation is also harder than the general ISRF.

4.2. Relationships between CO, A_B , and I_{100}

Assuming that optical extinction is proportional to dust column density (Hildebrand, 1983) and that the same dust component is well mixed with the gas (e.g. Bohlin, Savage, & Drake 1978), we use A_B as an estimator of total column density. We have determined the dependencies of ^{13}CO and infrared emission upon A_B for four clouds in the complex: L134, L1183, L1169, and L11780. The regression parameters obtained from least square fits are listed in Table 2. In the fits, we have considered $0 < A_B < 6$ mag, (JIC

higher cutoff for A_B has *been* introduced to avoid large weights to the least certain star count data (see discussion by Dickman and Herbst 1990; Laureijs et al. 1991). We ignored negative values of W_{13} . Since the zero level at 100 μm depends on the definition of the background, we did not impose any cutoffs in the infrared. In the following we write quantities that refer to averages over clouds between brackets.

Correlation diagrams of W_{13} versus A_B are displayed in Fig. 12. Of the four clouds, L1780 has the lowest degree of correlation with a correlation coefficient $R=0.65$. Although the scatter in the other objects is larger than expected from the uncertainties in the individual data points, the correlation diagrams show no evidence for deviations from linearity for $0 < A_B < 6$ mag. On the high extinction end, L183 shows a flattening in the relationship. From Table 2 we infer that the regressions in the three densest clouds do not significantly differ from each other. A weighted average for L134, L183, and L169 yields

$$W(^{13}\text{CO}) = (1.4 \pm 0.2) [A_B - (0.4 \pm 0.2)] \text{ K km/s}, \quad (1)$$

with A_B in mag. The relationship indicates the presence of a minimum extinction above which ^{13}CO is detected. The value of $\langle W_{13}/A_B \rangle$ is smaller in L1780. In addition, little ^{13}CO is detected for $A_B < 2$ mag.

The ^{13}CO column densities, N_{13} , have been estimated using the LTE analysis described by Dickman (1978). This method assumes CO opacities much higher than unity so that the excitation temperature can be derived from the observed $T_R^*(\text{CO})$. The ^{13}CO column density is obtained by assuming identical excitation temperatures for CO and ^{13}CO along each sightline. To investigate the relationship between N_{13} and total column density, we have plotted the ratio N_{13}/W_{13} as a function of A_B in Fig. 13. The value of N_{13}/W_{13} is actually determined by $T_R^*(\text{CO})$ and $T_R^*(^{13}\text{CO})$ in case both lines have identical linewidths. We have chosen to present the data in this form to investigate systematic variations when assuming LTE. Only values of $W_{13} > 0.3 \text{ K km/s}$ have been taken into account to avoid large random scatter due to small W_{13} . The correlations presented in Fig. 13 indicate that N_{13}/W_{13} exhibits a gradual increase as a function of increasing A_B . The variation in the trend is at most 20%. In the two clouds with highest opacity, L183 and L134, we observe a turnover: N_{13}/W_{13} flattens out for $A_B > 2$ mag and decreases with decreasing extinction for $A_B < 2$ mag. Consequently, we derive the average $\langle N_{13}/W_{13} \rangle$ for each cloud taking those data points with $A_B > 2$ mag (Table 3). The averages differ in the four clouds, increasing along with central extinction. We derive the weighted average for $A_B > 2$ mag:

$$\langle N_{13}/W_{13} \rangle = (1.32 \pm 0.07) 10^{25} \text{ cm}^{-2} \text{K}^{-1} \text{km}^{-1} \text{s} \quad (2)$$

and, in combination with equation (1):

$$\langle N_{13}/N(\text{H}_2) \rangle = (2.3 \pm 0.3) 10^{-6}, \quad (3)$$

where we assumed a constant gas to dust ratio of $\langle N(\text{H}_2)/A_V \rangle = 9.4 10^{20} \text{ cm}^{-2} \text{mag}^{-1}$ (Bohlin, Savage & Drake) and $A_B = A_V * (R+1)/R$ with $h = 3.1$ being the ratio total to selective extinction (Savage and Mathis, 1979).

Since the computation of N_{13} involves the ^{13}CO linewidth, N_{13}/W_{13} is independent of linewidth. Consequently, the observed variations in $\langle N_{13}/W_{13} \rangle$ probably are a result of variations in the adopted excitation temperatures derived from $T_R^*(\text{CO})$. We have measured the average value of $T_R^*(\text{CO})$ in the regions where $A_B > 2$ mag. These measurements together with the implied excitation temperatures are listed in Table 3. The temperatures are lower for the clouds with lower $\langle N_{13}/W_{13} \rangle$.

The correlation diagrams of I_{100} versus A_B are displayed in Fig. 14, and the derived regression parameters listed in Table 2. The diagrams of 1.183 and 1.1780 indicate a gradual flattening in the slope $\langle I_{100}/A_B \rangle$ suggesting a decrease of the 100 μm emission inside the clouds. 1.134 and L169 show no evidence for a possible flattening between $0 < A_B < 6 \text{ mag}$ on the observed scale of 6'.

4.2. ΔI_{100} and W_{13}

The analysis of the extended IRAS emission at 60 and 100 μm of 1.134, L183, and 1.1780 by Laureijs et al. (1991) has pointed out the existence of sudden variations in the 60 to 100 micron surface brightness ratio. It has also found that the quantity ΔI_{100} (defined below) exhibits a good linear correlation with ^{13}CO column density. However, the result was based on ^{13}CO data obtained from Snell (1981), which encompass a relatively small region in 1.183. We therefore repeat the analysis for the main clouds. Following Laureijs et al. (1991), we identify the 60 μm deficient regions by subtracting from the 100 μm map an emission component associated with the emission at 60 μm :

$$\Delta I_{100} = I_{100} - I_{60}/\Theta \quad \text{MJy/sr}, \quad (4)$$

where Θ is the ratio I_{60}/I_{100} in the outer parts of the cloud. The best value of Θ minimizes the amount of cirrus structure in the map of ΔI_{100} . We find $\Theta = 0.21 \pm 0.02$ in all clouds except L1780 where $\Theta = 0.27 \pm 0.04$. The resulting images of ΔI_{100} are presented in Fig. 15a-d. The similarity with the ^{13}CO images (Figs. 8 to 11) is striking.

Pixel to pixel correlation diagrams between ΔI_{100} and W_{13} for the four main clouds are presented in Fig. 16. The regression parameters obtained from the correlations between ΔI_{100} and A_B as well as ΔI_{100} and W_{13} have been included in Table 2. The diagrams exhibit tight relationships with correlation coefficients in excess of 0.82. The correlations in 1.183, L134, and L169 are to good approximation linear confirming the results of Laureijs et al. (1991). The parameters of the fitted regression lines (Table 2) show that $\langle \Delta I_{100}/W_{13} \rangle$ in these clouds are similar within the uncertainties. There is marginal evidence for a small threshold brightness ΔI_{100} below which no ^{13}CO is detected. The weighted average for these three clouds yields:

$$\Delta I_{100} = (1.43 \pm 0.08)[W_{13} - (0.3 \pm 0.2)] \text{ MJy/sr}. \quad (5)$$

Again, L1780 is significantly different from the other clouds, with $\langle \Delta I_{100}/W_{13} \rangle = 5.3 \pm 0.4 \text{ MJy/sr/(Kkm/s)}$, a factor 3.7 greater (corresponding to several sigma) than the average value given in equation (5). Also, the correlation diagram for 1.1780 indicates a non-linear relationship suggesting a stronger increase in W_{13} with increasing ΔI_{100} . Although $\langle \Delta I_{100}/W_{13} \rangle$ depends also upon Θ , the higher Θ in L1780 cannot account for the discrepancy. Taking $\Theta = 0.21$ for 1.1780 yields $\langle \Delta I_{100}/W_{13} \rangle = 4.1 \pm 0.7 \text{ MJy/sr/(Kkm/s)}$ which is still a factor 3 higher than in the other regions.

In Table 2 we list the regression coefficients for ΔI_{100} versus A_B . The ratios $\langle \Delta I_{100}/A_B \rangle$ for all clouds including 1.1780 are consistent within the uncertainties. The weighted average

$$\Delta I_{100} = (1.9 \pm 0.2)[A_B - (0.3 \pm 0.2)] \text{ MJy/sr}, \quad (6)$$

indicates that ΔI_{100} is only detectable above a threshold extinction of $A_B = 0.3 \text{ mag}$. This value is close to the threshold found for W_{13} versus A_B (cf eq. [1]). The fact that $\langle \Delta I_{100}/A_B \rangle$ in 1.1780 is not peculiar as

opposed to $\Delta I_{100}/W_{13}$ provides additional evidence that the deviation must be due to an anomalously low content of ^{13}CO emission in 1.1780 itself.

4.4. *Global density distributions*

Correlation diagrams have the disadvantage that they contain limited information about the brightness distributions of tracers. Extinction is a suitable probe to analyze the global density distributions of the main clouds due to its proportionality with column density. Since the clouds are sampled by pixels of equal size, column density profiles can be obtained by creating the cumulative pixel distribution as a function of decreasing extinction. The number of pixels at each value of A_B can be related to an area, and hence converted into an equivalent radius by assuming a regular cloud geometry. The distribution is normalized by dividing by the total number of pixels for the abscissa and by dividing by the upper 10th percentile brightness for the ordinate. For comparison, the distributions of ^{13}CO , ΔI_{100} , and I_{100} have been analyzed by using the same method. As an example we present the sorted data points for L183 in Fig. 17. Assuming spherical symmetry, we have fitted a power law density distribution to the observed extinction profile in Fig. 17.

The reliability of the analysis has been investigated by carrying out simulations in which noise was added to idealized profiles. We find that low signal to noise data ($s/n < 1$) tend to steepen the profiles at the ends as the high and low noise excursions will be sorted into the high and low bins, respectively. However, even a low signal to noise ratio of less than 6 for the maximum brightness value has little effect on the initial density distribution as the slope (in log-log space) remains the same over a large fraction of the profile.

Fig. 17 shows that the extinction profile of L183 closely resembles the functional form of an $r^{-1.1}$ density distribution. The 100 μm profile can be matched with a shallower distribution. The extinction profile is steeper at the high extinction end which is most likely due to the higher uncertainties in the extinction data. The results for the main clouds are listed in Table 4. The fitting procedure has been performed in log-log space. The exponents of the density distributions show relatively little variation, all lying between -1.1 and -1.6. The extinction profiles for 1.169 and 1.183 are nearly identical whereas both L134 and L1780 have a significantly lower exponent. Similar to the profiles of L183, the 100 μm profiles of the other clouds show a more gradual decline with increasing area. In contrast to the extinction and far-infrared profiles, ^{13}CO brightness distributions in L134, L169, and L183 do not show much evidence for a single power-law density distribution. The profiles exhibit a shallow distribution for roughly the brightest 50% of the area (exponents spanning a range from -0.5 to -1.5) and the profiles steepen in the outer regions resembling an r^{-2} density distribution. The ^{13}CO profile of L183 in Fig. 17 is a typical example. Only in L1780, the ^{13}CO profile can be fitted with an r^{-2} density distribution over its entire region.

4.5. *^{13}CO versus C^{18}O*

Among other parameters, the strength and direction of the radiation field affect the emission of carbon monoxide by means of photo-dissociation of the molecule. Since ^{13}CO and C^{18}O have different abundances, self-shielding occurs at different depths making the ratio W_{13}/W_{18} a diagnostic for the penetration depth of the UV field. The values for W_{13}/W_{18} in L134 and L183 as a function of A_B have been plotted in Fig. 18.

The data in Fig. 18 show that W_{13}/W_{18} exhibits a broad range of possible values for each extinction value along the line of sight. The large span of ratios at a given A_B can be attributed to the displacement of the ^{13}CO morphology with respect to that of C^{18}O . This effect is illustrated in Fig. 19d (see also section

4.6. below). The distributions of the data points for L134 and L183 are similar: (the highest ratios W_{13}/W_{18} are distributed around $A_B = 4$ mag).

Following the work by van Dishoeck & Black (1988), we define the column density ratio R_N normalized by the relative abundances of the isotopes

$$R_N = N_{13}/N_{18} * [C]/[^{13}C] * [^{18}O]/[O], \quad (7)$$

where the brackets denote the absolute abundances of the atomic species. In the idealized case, the value of R_N should approach unity in high opacity regions where UV starlight is absent. We have adopted abundance ratios of $[C]/[^{13}C]=45$ and $[O]/[^{18}O]=500$, in accordance with the values used by van Dishoeck and Black. The $C^{18}O$ integrated intensity has been converted to column density using the relationship presented by Swade (1989b)

$$N_{18} = 8.27 \cdot 10^{14} W_{18} \quad \text{cm}^{-2}, \quad (8)$$

where an excitation temperature of 9 K was assumed to compute the fractional population density in the $J=1-0$ state under LTE conditions. To convert W_{13} to N_{13} , we applied the averaged observed value for N_{13}/W_{13} given in eqn (4.2.2.). This way the ratio W_{13}/W_{18} is proportional to R_N . The values for R_N are given on the right vertical axis in Fig. 18. We see that R_N comes close to unity for $A_B > 6$ mag. The maximum observed value of R_N is about 4.

4.6. WV Anisotropy

In Fig. 19 are plotted the variations of the different tracers along a slice through the center of L134. The orientation of the slice has been chosen in such a way that it approximately points to the direction of the Sco OB2 association. The radiation field is expected to decrease monotonically towards positive offsets along the slice with the maximum possible contrast. The center of the slice (position O) is about 1' south of the position of the ammonia core (at RA=15^h51^m00^s, Dec=-4°30') listed by Benson & Myers (1989). The variation of A_B which is the best column density tracer independent of the UV radiation field, is given in panel c. The extinction at O' is a lower limit.

The variations of I_{12} and I_{25} are presented in Fig 19a. The zero level of the slices with respect to L134 is uncertain to about 0.2 MJy/sr. An emission minimum is observed at position O accompanied by two peaks on either side. The maximum on the illuminated side (i.e. the SE side) peaks at $A_B = 2$ mag and is almost twice as bright as the peak on the shadow side which occurs at $A_B < 1$ mag. The 12 and 25 μm emission remains relatively high (0.2–0.3 MJy/sr above the lowest brightness point) at positions well outside the densest regions of the cloud where A_B is less than 1 mag. On the illuminated side the 12 and 25 μm emission extends to more than 10' away from the cloud center, whereas on the shadow side the emission drops below 0.1 MJy/sr at 40'' from the center. Thus I_{12} and I_{25} are both brighter and more extended on the side of the cloud which faces the UV field.

The emission at 60 and 100 μm declines rapidly away from the cloud's center (Fig 19b). The 100 μm emission exhibits a peak at -13', well away from the ammonia core, but a local maximum can be distinguished at position O. The maximum of I_{60} is also on the illuminated side. The striking drop in I_{60} at -17' was reported by Laureijs et al. (1991). On the shadow side of the cloud there is little 60 μm emission and no evidence for a secondary emission peak as seen at 12 and 25 μm . The difference between the 60 and 100 μm slices defines ΔI_{100} and is presented in panel c. The profile of ΔI_{100} is similar to the

extinction profile and has a second peak at the ammonia core.

Of the three far-infrared brightness ratios shown in panel f, the ratio I_{12}/I_{25} is the most constant. I_{12}/I_{25} is everywhere close to 1.0; high excursions at positions $-4'$ and $+8'$ have high uncertainties due to the low surface brightness values at 12 and 25 μm . Both other ratios, I_{12}/I_{100} and I_{60}/I_{100} , show a dip in the cloud center. None of the three ratios exhibit an obvious dependence on the *direction* of the radiation field. The same is observed for I_{100}/A_B (Fig. 19g). Although there is a clear minimum at the position of the ammonia core, the ratio resumes a value of 4-6 MJy/sr/mag in the outer regions at both sides of the cloud. However, I_{100}/A_B exhibits a gradual *increase* towards the shadow side.

The morphologies of CO, ^{13}CO and C^{18}O are markedly different from each other (Fig. 19c). CO peaks at the same position as the 100 μm emission and shows no evidence for the presence of the ammonia core. The same is observed in ^{13}CO , the peak in the ^{13}CO distribution occurs at a somewhat higher extinction. The ammonia core lies on the declining flanks of the CO and ^{13}CO profiles on the shadow side of the cloud. In contrast, C^{18}O peaks closely to the ammonia core. Consequently, W_{13}/W_{18} (Fig. 19h) is high on the illuminated side and remains low on the shadow side. The ratio displays a maximum of 23 around $-11'$, a sharp drop to a minimum of 4 at $2'$ and a small local maximum at $8'$.

We have plotted $T_R^*(\text{CO})$ in Fig. 19d to obtain an impression of the variation of the gas temperature along the slice. Presumably, CO is not optically thick for offsets less than $-12'$ and greater than $9'$. From position $-20'10''$ to $+10'$, $T_R^*(\text{CO})$ gradually decreases from about 16 K to 10 K. Assuming the CO optically thick and thermalized in these regions, we infer that the kinetic temperature of the gas correspondingly should drop 7 K, from 20 K on the bright side down to 13 K on the shadow side of the cloud. The drop in T_R^* is less steep than the decline in W_{12} indicating that the lines are both weaker and narrower on the shadow side of the cloud.

A slice through the translucent cloud L1780 with the same orientation as that of L134 has been plotted in Fig. 20, to investigate the differences between the tracers in case the cloud's central opacity is low (center $A_B = 4.4$ mag). We observe qualitatively similar variations in L1780 as for L134, the difference is that the center of L1780 is not sufficiently dense and opaque to give rise to strong C^{18}O and detectable ammonia emission. Compared with L134 and L183, the infrared emission in L1780 is significantly brighter at 25, 60, and 100 μm . The 60 and 100 μm profiles are asymmetric and peak at the same position as the carbon monoxide lines. The infrared brightness ratios (panel f) I_{12}/I_{25} and I_{60}/I_{100} decline towards the shadow side and there is no indication that they return to their initial value. This is probably due to the strong decline in infrared emission on the shadow side which indicates a complete absence of an extended diffuse cloud layer which is still present in the outer regions of L134.

The CO emission in L1780 is weaker than the corresponding slices in L134. In contrast to L134 the profile of $T_R^*(\text{CO})$ in L1780 is highly symmetric. However, the lines are narrower on the shadow side (cf. W_{12} and $T_R^*(\text{CO})$ in Figs. 20c and d, resp.).

In conclusion, the asymmetric profiles of $T_R^*(\text{CO})$ and W_{13}/W_{18} in L134 indicate anisotropic illumination by the external UV field. The molecular lines are narrower on the shadow side of L134 and L1780. The infrared brightness profiles in L134 and L1780 are consistent with the notion that the clouds have a larger extended diffuse layer on the illuminated side.

4.7. Properties of ^{13}CO Clumps

The velocity maps displayed in Fig. 7 indicate the presence of individual cloud components which could be isolated both in velocity and map space. We analyze these clumps to probe both their interiors as well as the medium in which they are immersed. Since the clumps are all at the same distance, a sample can

be constructed on a well-defined size and luminosity scale.

Maps of ^{13}CO with 0.4 km/s velocity separation, 3x3 arcmin sampling, and smoothed to an effective resolution of 3.4 arcmin were used. Analogous to the procedure of Solomon et al. (1987), we define clumps as topologically closed surfaces of constant antenna temperature T_{R}^* in x, y, v space in which T_{R}^* exceeds a given threshold temperature. This definition allows more than one emission maximum within a clump boundary. A threshold temperature of $T_{\text{R}}^* = 1.6$ K has been adopted because this temperature yields the highest number of individual clumps. Higher threshold temperatures ignore a significant fraction of the weaker clumps, whereas lower temperatures cause a stronger blending between the features. A temperature of 1.6 K corresponds to about 4 times the r.m.s. noise per pixel in the velocity maps. A few clouds, notably the filaments in L169 show blending just above the threshold level. Since separate clumps could clearly be distinguished within these clouds, we have split the features along the borders of minimum emission. The majority of the clumps have sharp edges in ^{13}CO . This is confirmed by the average T_{R}^* of a clump which generally exceeds 2.0 K, well above the threshold temperature.

We determined the area S of a clump by projecting it onto the x, y -plane. The equivalent radius R_{eq} is derived from the usual expression $S = \pi R_{\text{eq}}^2$. Let $w(v) = \int T_{\text{R}}^*(v) ds$ be the ^{13}CO emission integrated over the area $S(v)$ in a particular velocity interval. The velocity width ΔV is determined from

$$\Delta V = 0.94 \sum_v w(v) / \max(w(v)) \quad \text{km/s}, \quad (9)$$

where $\max(w(v))$ is the peak integrated emission, the factor 0.94 makes ΔV equivalent to the FWHM of a gaussian profile. By adopting this method we only consider the velocity contribution of the material associated with $T_{\text{R}}^* > 1.6$ K to determine ΔV . The velocity of a clump is calculated from the intensity weighted mean

$$V = \sum_v v w(v) / \sum_v w(v) \quad \text{km/s}. \quad (10)$$

The position of a clump has been determined from the emission centroid in the channel centered on V . The CO and ^{13}CO temperatures of a clump have been estimated from the temperature averaged over the area in the same velocity channel.

Assuming optically thick CO lines we derive the mean kinetic temperature, T_{K} , of a clump by measuring the average CO temperature in the area at peak velocity. This parameter is then used to compute the thermal velocity dispersion for the mean particle, σ_{gas} , which is higher than the dispersion of the relatively massive trace molecule (e.g. Myers 1983):

$$\sigma_{\text{gas}}^2 = k T_{\text{K}} (1/m_{\text{gas}} - 1/m_{^{13}\text{C}}) \quad (\text{km/s})^2, \quad (11)$$

where k is Boltzmann's constant, $m_{^{13}\text{C}}$ and m_{gas} are the masses of a ^{13}CO molecule (29 a.m.u.) and the average mass of a gas particle (7/3 a.m. u.), respectively.

The mass of a clump can be derived by considering a linear regression between A_{B} and $W_{^{13}\text{CO}}$ as observed in 1.134, 1.169, and 1.183. Assuming that equation (1) applies to the clumps, then the mass of a clump is proportional to $L(^{13}\text{CO})$:

$$M_{^{13}\text{CO}} = (9.7 \pm 0.3) L(^{13}\text{CO}) \quad M_{\text{sun}} \quad (12)$$

where $L(^{13}\text{CO})$ is expressed in units of K km/s pc^2 .

We have determined a total of 18 clumps, the measured quantities and the derived parameters are presented in Tables 5a and 5b, respectively. The size-CO-luminosity relationship as well as the size-linewidth relationship for the L134 complex of clouds are displayed in Figs. 21a and b. We observe clear correlations in both relationships. Least squares fits in log-log space with R_{eq} (in units of pc) as the independent x-variable yield the following regressions:

$$\Delta V = (1.8 \pm 0.4) * R_{\text{eq}}^{(0.51 \pm 0.07)} \quad \text{km/s}, \quad (13)$$

and

$$L(^{13}\text{CO}) = (1.2 \pm 0.2) * R_{\text{eq}}^{(2.58 \pm 0.06)} \quad \text{K km/s pc}^2, \quad (14)$$

or

$$M_{13} = (1.2 \pm 0.2) * 10^2 * R_{\text{eq}}^{(2.58 \pm 0.06)} \quad M_{\text{sun}}, \quad (15)$$

with correlation coefficients $|R|$ of 0.89 and 0.99, respectively. Equations (12) and (14) have been combined to obtain equation (15), the six-mass relationship. The total mass contained in the ^{13}CO clumps is $80 M_{\text{sun}}$ with 40% of the mass in the two clumps associated with the ammonia cores.

5. Interpretation

5.1. CO column density

The comparison between ^{13}CO column density and extinction (sect. 4.2) yields an average ratio

$$\langle N_{13}/A_V \rangle = (2.4 \pm 0.3) * 10^{22} \quad \text{cm}^{-2} \text{mag}^{-1}, \quad (16)$$

which is in agreement with previous determinations of this ratio (Bachiller and Cernicharo, 1986). Dickman & Herbst (1990) found a similar result for the ρ -Oph region, $\langle N_{13}/A_V \rangle = (2.2 \pm 0.1) * 10^{22} \text{ cm}^{-2} \text{mag}^{-1}$, using a similar CC analysis but extinction data obtained from photographic plates taken in the N band ($\lambda = 8000 \text{ \AA}$). In view of the uncertainties in the conversion from star counts to extinction and subsequently to A_V , which are difficult to quantify, the two results are in good agreement. Since Dickman & Herbst measured the relationship in very obscured regions up to $A_V = 15 \text{ mag}$, whereas our result strictly derives from relatively low extinction regions ($1.5 < A_V < 5 \text{ mag}$) we infer that the ratio applies over a large range of column densities. As noted in section 3.1, the ρ -Oph complex is associated with the L134 complex of clouds suggesting that the CO isotopic composition in both complexes is similar.

The value for the threshold extinction ($A_V = 0.3 \pm 0.1 \text{ mag}$) determined from the correlation between A_B and W_{13} is lower than the threshold found by Dickman & Herbst from the regression in A_V versus N_{13} ($A_V = 1.42 \pm 0.40 \text{ mag}$). The drop in N_{13}/W_{13} with decreasing A_B (sect. 4.2) could raise the threshold but not enough to explain the difference. It is more likely that the discrepancy is due to the fact that we did not include the low density material in which the clouds L134, L169, and L183 are embedded (sect. 3.1). The star counts do not trace large scale offsets at low level, because the limited size of the photographic plate forced the reference field (which defines the zero level) to lie inside the extended structure. The photometric measurements by Franco (1989) suggest $E(b-y) = 0.2$ for the halo, which corresponds to

$A_V=0.8$ mag adopting the conversion given by Crawford & Mandwewala (1976), $E(b-y)=0.74E(B-V)$ for $R=3.1$. Thus the ^{13}CO regions in the densest clouds are only detectable above a threshold extinction of about $A_V=1.1$ mag, in accordance with Dickman & Herbst.

The integrated line intensity is proportional to the total number of emitting molecules along the line of sight if the line is not saturated and T_{ex} is constant. The correlations between W_{13} and extinction (Fig. 12) are best fitted by straight lines suggesting that the ^{13}CO lines are indeed optically thin, particularly in the low extinction regions. At the highest opacity ends in L134 and 1,183 ($A_B > 6$ mag), a flattening in the relationship occurs. As discussed in the following sections, the high opacity regions reside in the WV shielded parts of the clouds. The flattening therefore is likely due to a combination of a lower excitation temperature and saturation of the ^{13}CO lines in the high opacity cloud centers.

At the low extinction end, the analysis of N_{13}/W_{13} (sect. 4.2) implies subtle differences between correlation diagrams of W_{13} versus A_B and N_{13} versus A_B . Because ^{13}CO is likely to be optically thin for $A_B < 2$ mag, the diagrams in Fig. 13 indicate that N_{13} is systematically underestimated by at most 20% at the low extinction edges of dense clouds.

The underestimation might be due to a low CO opacity so that the CO brightness temperature does not reflect the excitation temperature. However, the CO optical depths obtained by multiplying the ^{13}CO optical depths by the abundance ratio $[\text{C}]/[^{13}\text{C}]$ (i.e. $\tau(\text{CO}) = -4.5 \ln[1 - T_{\text{R}}^*(^{13}\text{CO})/T_{\text{R}}^*(\text{CO})]$) indicate optically thick CO emission for any sightline where ^{13}CO has been detected. An alternative explanation for the underestimation would be the presence of unresolved structures with a low beam filling factor in addition to a resolved diffuse cloud component. The observed CO temperatures will be lower but opacity estimates are less affected as these are derived from temperature ratios.

The average CO temperatures for $A_B > 2$ mag (Table 3) for L134, 1,183, and 1,169 are nearly equal. The inferred excitation temperatures are about 15 K. The constancy of the excitation temperature for $A_B > 2$ mag indicates that the CO lines are optically thick and thermalized.

L1780 exhibits different properties. In Table 3 the value for T_{ex} in L1780 is lower but the temperature variation along the slice in Fig. 19d indicates that CO has not reached saturation in this cloud. Thus the derived T_{ex} is underestimated from the brightness temperature. The ratio W_{13}/A_B (Table 2) shows that the ^{13}CO content in L1780 is low (cf Figs. 12 and 13). This is supported by $\Delta I_{100}/A_B$ which is comparable to the ratio in the other clouds, whereas $\Delta I_{100}/W_{13}$ is almost a factor 4 larger. Using the values of Table 3 we derive an average value of

$$N_{13}/A_V = (0.5 \pm 0.2) 10^{15} \quad A_V < 3.3 \text{ mag}, \quad (17)$$

which is about a factor 4 lower than (5.1.1). The lower ^{13}CO content of L1780 is likely associated with the relatively low opacity of L1780. The UV radiation field can penetrate into a large volume fraction of the cloud thereby photo-dissociating a fraction of the ^{13}CO in the very cloud center.

From the observations we conclude that ^{13}CO is a good estimator of column density, and that $\langle N_{13}/N(\text{H}_2) \rangle$ settles to a unique value in regions that are completely opaque to UV radiation such as L134, 1,183, L169 and the dense Ophiuchus clouds studied by Dickman & Herbst. The value for $\langle N_{13}/N(\text{H}_2) \rangle$ is substantially lower in low opacity clouds not embedded in an extended structure, as is the case for L1780.

5.2. $^{13}\text{CO}/\text{C}^{18}\text{O}$

Comparison of the observed ratio W_{13}/W_{18} for 1,183 and 1,134 (Fig. 15) with theoretical predictions such as those published by van Dishoeck & Black (1988) reveals several noticeable aspects:

1. According to Fig. 18 the observed peak in R_N is at $A_B=4$ mag ($A_V=3.0$ mag). This translates to a total visual extinction of $A_V=3.0+0.8=3.8$ mag, if we include the extinction contribution of the filament in which the clouds are embedded. The model calculations predict the peak in R_N to occur at $A_V<1$ mag in the case of a plane parallel cloud and a normal ISRF. The actual geometry of the cloud could increase the extinction value at peak W_{13}/W_{18} (Glassgold, Huggins & Langer 1985), but considering the observed global density distributions ($r^{-1.2}$) found in section 4.4., we expect at most a factor 2 and not a factor 4 discrepancy.

2. The maximum value of R_N is about 4.2. Assuming a carbon depletion factor of 0.4 (i.e. 40% of the cosmic carbon abundance in the gas phase), Van Dishoeck & Black predict peak values of $R_N=10$ and 20 for $T_k=50$ and 15 K, respectively. However, our observations (Table. 3) rule out kinetic temperatures that are much higher than 15 K, suggesting that the predicted peak in R_N is too high by a factor 5 or more.

3. If the peak in R_N is caused by fractionation, the observed low ratios over the whole range of A_B suggest that fractionation is much less pronounced on the shadow side of the clouds. This effect is also demonstrated in Fig. 19. A lower kinetic temperature on the shadow side, of the clouds would in theory increase R_N since fractionation of ^{13}CO causes the peak to rise when the kinetic temperature is lowered. We conclude that the low ratio must be due to a combination of the lower UV field, a high carbon depletion, and a steep density gradient which makes a possible fractionation peak unresolvable.

Van Dishoeck & Black pointed out that an increase in the strength of the UV field lowers the peak R_N and shifts it towards higher opacities. Although the radiation field in the complex is higher than average (Sect. 4. 1.), this mechanism can only partly explain the observations as the peak is not predicted to decrease to a value as low as observed. Alternatively, a higher carbon depletion lowers the peak proportional to the depletion, and shifts the peak towards higher opacities due to the reduced UV shielding by molecules. A quantitative comparison with the models shows that a carbon depletion factor of about 0.1 (as opposed to a standard value of 0.4) is necessary to match the models with the observations. A similar value of the carbon depletion factor is inferred by van Dishoeck & Black from ^{13}CO observations near $\rho\text{-Oph}$.

A carbon depletion factor of 0.1 as an interpretation for the general shape of Fig. 18, is consistent with the derived value for $N_{13}/N(\text{H}_2)$ in equation (3). Taking $[\text{C}]/[^{13}\text{C}]=45$, a carbon abundance of $[\text{C}]=4.68 \cdot 10^{-4}$, and assuming that all molecular carbon originates from gas phase carbon atoms, we derive a gas phase carbon abundance of 0.1. One should keep in mind that the consistency might be fortuitous: firstly, the assumed value of $[\text{C}]/[^{13}\text{C}]$ is subject to debate and could be twice as much (Crane, Hegyi & Lambert 1991), and, secondly, the ratio $N_{13}/N(\text{H}_2)$ is likely to be non-uniform along the line of sight.

The diagram of W_{13}/W_{18} versus A_B (Fig. 18) is similar to the one presented by Langer et al. (1989) who plotted R_N as a function of N_{13} in the analysis of dark cloud B5. The large variation of R_N in their diagram also suggests that the radiation field in B5 is far from isotropic although the irregular geometry of B5 might contribute to an enhanced scatter.

In conclusion, the relationship between W_{13}/W_{18} and A_B in both L134 and L183 is consistent with a carbon depletion of 0.1, possibly combined with an enhanced radiation field. The anisotropy of the radiation field increases the scatter in W_{13}/W_{18} at a given A_V .

5.3. Dust Temperatures

Any realistic dust model predicts dust equilibrium temperatures T_d of less than 18 K for the large grains exposed to the general ISRF (see e.g. Draine 1990). This means that the corresponding ratio I_{60}/I_{100} must be less than about 0.06. As I_{60}/I_{100} is about 0.2 or larger for the diffuse interstellar medium, a large fraction

of the 60 μm emission must be due to a different dust component. Thus ΔI_{100} as defined in equation (4) corresponds to the regions where the emission from dust other than the large grains is absent.

The pixel to pixel correlations between ΔI_{100} and A_B (not shown) exhibit no strong deviations from linearity. The correlation coefficients for $\langle \Delta I_{100}/A_B \rangle$ do not differ greatly from those of $\langle I_{100}/A_B \rangle$ (Table 2). The values of $\langle \Delta I_{100}/A_B \rangle$ obtained from regression analysis are similar for all clouds in this study, including 1.1780. Since A_B is proportional to column density, this result suggests that ΔI_{100} is a good column density tracer for $A_B < 6$ mag. Since the infrared emission depends not only on the total column density but also on the temperature of the grains, the constancy of the mean ratio $\langle \Delta I_{100}/A_B \rangle$ amongst clouds implies that the dust temperature giving rise to ΔI_{100} has the same value from cloud to cloud.

The ratio $\Delta I_{100}/A_B$ shows a gradual increase towards the shadow sides of L134 and L1780 (sect 4.6). This means that either the emissivity of the ΔI_{100} regions is higher at 100 μm or that the amount of very cold dust with respect to the warmer dust associated with I_{60} along the line of sight increases towards the shadow side of the cloud. The first interpretation would imply that the dust is warmer on the shadow side of the cloud, contradicting the other observations. The second explanation is more likely and implies that (i.) the more diffuse and warmer dust is much more extended at the UV side of the cloud, and (ii.) the straight ratio $\Delta I_{100}/A_B$ (i.e. not the average ratio obtained from regression analysis) is a poor tracer of temperature variations but a good tracer of column density in regions associated with ΔI_{100} .

The absence of 60 μm emission in the ΔI_{100} regions yields an upper limit of $T_d < 15$ K (assuming a λ^{-1} emissivity; steeper emissivities yield lower T_d) for the dust associated with ΔI_{100} (Laureijs et al. 1991). An alternative temperature constraint for the regions sampled by ΔI_{100} is provided by the gas kinetic temperature T_k . At sufficiently high densities, CO will be thermalized and T_{ex} becomes identical to T_k . Model calculations by Falgarone & Puget (1985) who included in their calculations a density distribution and the cooling by dust, predict that $T_k < T_d$ in regions with densities of order 10^3 – 10^4 cm^{-3} . In those regions the UV field is sufficiently diminished making it unable to heat the gas efficiently through photoionization whereas the densities are still too low for effective heating by the dust. Thus the gas kinetic temperature should serve as a lower limit for the dust temperature. Excluding 1.1780, we find $T_k = 14$ – 17 K for the densest clouds (Table 3). From the ^{13}CO clumps we estimate a typical density of 10^3 cm^{-3} (Table 5b) for the regions related to ΔI_{100} . The observed T_k and the upper limit $T_d < 15$ K suggests that the physical dust temperature must be close to 15 K in regions of ΔI_{100} . This conclusion was also reached by Laureijs et al. (1991) based upon other reasons.

The absence of strong 100 μm emission associated with the ammonia core in L134 (Fig. 19b) suggests a dust temperature lower than the T_d in regions of ΔI_{100} . As indicated by the CO temperatures in Fig. 19, T_k drops accordingly.

5.4. Infrared colors and the radiation field

The ratio I_{60}/I_{100} in 1.1780 is higher than in the other clouds (0.27 as opposed to 0.22). According to model calculations by Désert et al. (1990) this ratio can be realized by scaling the UV part of the radiation field ($0.09 < \lambda < 0.30$ μm) to 4 times the Mathis et al. (1983) ISRF. This result agrees with the predicted strength of the radiation field derived from the UV sources near the 1,134 complex (sect. 4.1). The UV enhancement would also affect the 100 μm emission. The corresponding predicted value of I_{100}/A_B is 60 MJy/sr/mag. The observed value of $\langle I_{100}/A_B \rangle$ in 1.1780 is an order of magnitude lower (5.9 ± 0.5 MJy/sr/mag), but the I_{100} vs A_B correlation diagram does not rule out an initial slope of 60 MJy/sr/mag for $A_B < 1$ mag where all UV absorption should take place (Fig. 14). Thus as indicated by the infrared maps and confirmed by I_{60}/I_{100} , there is little or no dust between the heating sources and L1780. The

diffuse extended region surrounding the other clouds is sufficient to decrease the strength of the UV component with a factor 4 or more since I_{60}/I_{100} in the other clouds is normal. This decrease is consistent with the total extinction of the extended region ($A_V=0.8$ mag, sect. 5.1)

The 25 μ m emission in L1780 along the slice displayed in Fig. 20a indicates a distribution different from I_{12} and more related to I_{60} . Support for this observation is provided by I_{12}/I_{25} (Fig. 20f) which is on average lower than in L134 and shows a significant decrease from 0.8 to 0.4 on the shadow side of L1780. Thus I_{25} in L1780 has a mixed character: it displays properties seen in both the 12 and the 60 μ m IRAS bands. The mixed character is qualitatively consistent with the three component grain model of Désert et al. (1990) where an attenuation of the ISRF through a slab of $A_V=1$ mag causes a drop from 0.83 to 0.62 in I_{12}/I_{25} . This is due to a relatively stronger emissivity of the very small grain component which is predominant in the 60 μ m band.

5.5. Clumps and Stability

Both the exponent as well as the scaling constant in the observed size-linewidth relationship are in agreement with previous studies of dark clouds (Leung et al. 1982; Myers 1983) and giant molecular clouds (Solomon et al. 1987; Scoville and Good 1989), despite the fact that these studies involve different trace molecules and different clump definitions. All these studies have in common that they impose a fixed brightness to define the boundaries of the clumps. The agreement suggests that the size-linewidth relationship is scale free, i.e. there is no unique boundary in the cloud for which the relationship holds.

observations of ^{13}CO clumps in a quiescent region in the Cep 0133 molecular cloud by Carr (1987) have indicated a size linewidth relationship with an exponent of 0.24, but the correlation coefficient (0.58) found by Carr is lower than ours. Combination with our data shows that the smaller clumps in Carr's sample have systematically higher values for A_V . This may be attributed to the coarser velocity resolution ($\Delta v=0.8$ km/s) used by Carr. We therefore believe that the size-linewidth relationships in the two ^{13}CO datasets are not different.

The exponent in the size-luminosity relationship (eq. [14]) is in excellent agreement with the exponent in the size-mass relationship obtained by Carr (1987; exponent=2.51 \pm 0.06) in Cep 0B3 and Casoli et al. (1984) in Orion and Perseus. Malony (1989) pointed out that such a power law could easily be explained if one considers the empirical size-linewidth law and the fact that the temperature of the CO line is nearly constant. Assuming $L(^{13}\text{CO}) \propto R_{\text{eq}}^2 \langle T_R \rangle \Delta v$ and substituting $\Delta v \propto R_{\text{eq}}^{0.5}$, we obtain $L(^{13}\text{CO}) \propto R_{\text{eq}}^{2.5} \langle T_R \rangle$ which is in accordance with the observations.

As a consequence, studies that find a significantly different exponent in the size-linewidth relationship, will obtain a different size-luminosity (or size-density) relationship. The observations of the Ophiuchus dark cloud complex by Loren (1989a, b) show evidence that the sizes of the clumps are poorly correlated with linewidth. Moreover, Loren finds masses that are proportional to R_{eq}^3 , which implies that the density in the ^{13}CO clumps is constant. The fundamental difference between our measurements and those of Loren is that Loren did not permit more than two emission peaks in one clump except in regions where the ^{13}CO lines show high optical depths. This requirement relaxes the constraint of a fixed boundary level as the boundaries were defined by following the minimal temperature contour. His method tends to minimize the velocity width of the most massive clumps (according to our definition) by splitting these into smaller entities.

The stability of the clumps can be analyzed by evaluating the terms that enter into the virial equation for clouds (Keto & Myers, 1987). The gravitational and turbulent energy of a clump and the surface and magnetic pressure acting upon a clump are related via

$$|E_{\text{grav}}| - E_{\text{turb}} = E_{\text{pres}} + E_{\text{mag}},$$

from which follows:

$$GM^2/R - M\sigma_{\text{tot}}^2 \ln 2 = p_0 R^3 \quad \text{erg}, \quad (18)$$

where $\sigma_{\text{tot}}^2 = \sigma_{\text{gas}}^2 + \sigma_{\text{turb}}^2$. It is assumed that the clumps have an internal density distribution proportional to r^{-2} . In the second equality we have lumped together the contributions of the boundary and magnetic field pressure into a single parameter, p_0 , the total pressure. This quantity describes the forces that are necessary to prevent the clump from expanding.

The values for E_{turb} and E_{grav} in Table 5b show that the turbulent energy is always larger than the gravitational energy, and that E_{turb} is at least a factor 8 larger for all but the three most massive clouds. The empirical relationships given in Section 4.7. yield $E_{\text{grav}}/E_{\text{turb}} = 0.5R^{0.56}$, where R is in pc. According to this expression - when ignoring the pressure term - the ^{13}CO clouds are in virial equilibrium if their radii are of order 1 pc or larger.

The observed linewidths are predominantly due to line broadening by turbulence. The values for p_0 are in the range $1 \cdot 10^{-4} - 7.104 \text{ cm}^{-3}\text{K}$ with a median value of $2.104 \text{ cm}^{-3}\text{K}$. The smaller clumps, where the E_{grav} is small compared to E_{turb} , have more similar pressures.

6. Discussion

6.1. Physical conditions inside moderate density regions

The images of ΔI_{100} offer the possibility to "clean" the $100 \mu\text{m}$ images of the foreground and background emission regions where the UV field is still present. This hypothesis is supported by the clear correlations between ΔI_{100} and W_{13} and our analysis in sect. 5.1 which shows that ^{13}CO becomes widespread in clouds only after A_V exceeds 1.2 mag. Consequently, the $60 \mu\text{m}$ emission must be anti-correlated with ^{13}CO , and the images of I_{60} must trace the diffuse UV component which photodissociates ^{13}CO . The constancy of both $\langle \Delta I_{100}/A_B \rangle$ and $\langle W_{13}/A_B \rangle$ indicates that the dust temperature in the regions of ΔI_{100} must be reasonably uniform except in the high opacity regions where $A_B > 6$ mag.

The constancy of $\langle \Delta I_{100}/W_{13} \rangle$ for all clouds except L1780 makes plausible that the physical conditions are similar in the regions where ΔI_{100} is significant. These regions are protected from the UV field that determines the outer cloud conditions which could vary from cloud to cloud due to local shadowing of the ISRF. Once inside, the environments in the dense clouds become more similar in temperature, densities, and ^{13}CO abundances. L1780 is an intermediate case: according to photometric measurements the cloud lacks a diffuse halo and the total opacity of the cloud is such that the radiation field is still affecting the molecular content.

The uniformity of ΔI_{100} implies that temperature variations delineated by changes in $\langle I_{100}/A_B \rangle$ must occur in the outer cloud regions where I_{60} and therefore the UV field is still present. The tight linear relationships both for I_{100} versus A_B and as well as for ΔI_{100} versus A_B can be explained by assuming that the $60 \mu\text{m}$ deficient regions are well mixed and relatively small compared to the regions associated with I_{100} . The $r^{-1} - r^{-1.5}$ density distributions (section 4.4) and the amount of ^{13}CO clumps are indicative for a clumpy cloud structure. Exceptions are the northern tip of L183 where the $60 \mu\text{m}$ deficient region is large

and 1.1780 where we detected only one ^{13}CO c-lump. In these regions we observe a significant flattening in I_{100} versus A_B (Fig. 14).

In section S.3. we argue that the temperature of the dust must be close to that of the gas in the 60 pm deficient regions (or ^{13}CO clouds). The inferred dust temperature is higher than expected from cosmic ray heating alone, which suggests that dust associated with ^{13}CO regions is predominantly heated by the external radiation field. The clump analysis (section 4.7 and 5.5) has shown that these regions can be characterized by densities $n(\text{H}_2)$ of order a few times 10^3 cm^{-3} and boundary pressures of order $p_0/k=4 \cdot 10^4 \text{ K cm}^{-3}$.

6.2. *The anisotropic UV field: shielding of the dense cores*

The molecular, infrared, and the extinction data clearly exhibit a regular pattern in the main clouds L183, 1.134, L] 69, and L] 780. The diffuse material is found to be widespread on the eastern and southern sides of the clouds, whereas the dense cores are found on the opposite side, due north-east. The gas temperature derived from the CO lines shows a gradient along the same direction. The variation of the ratio W_{13}/W_{18} is indicative of a highly anisotropic UV radiation field. These measurements are consistent with the position of the main UV sources (Sco-OB2 and ζ Oph) with respect to the L134 complex (sect. 4.1). The alignment along the direction of the UV field of the density gradient and the major symmetry axes of the elongated clouds readily suggest a physical connection. In the following we argue that the position of the densest regions in L] 34 and L] 83 as well as the morphology of the complex can be explained by the strength and the direction of the UV field.

A full treatment of the hydrostatic equation of state of a molecular cloud excluding magnetic fields has been carried out by Falgarone & Puget (1985). In this model, the structure of a cloud can be separated into three regions: 1. an isothermal core, 2. an intermediate layer in which the density is lower and the UV shielding is reasonable, and 3. a halo where the gas is heated indirectly by the UV field. The structure of a condensation depends only on two physical parameters: the central density of the core and the external UV radiation field. The temperature of the dense core is determined by the temperature of the dust.

A consequence of the halo is that it acts as an absorbing layer protecting the core from the external radiation field. The gas temperature of the core depends on the dust temperature, and is weakly sensitive to the strength of the UV field. We have seen in the previous section that a similar mechanism governs the temperature of the dust inside clouds. Substantial variations in the UV field affect only the outer cloud regions and the temperature of the central regions is nearly constant for a large range of models.

Although the model by Falgarone & Puget assumes spherical symmetry and a homogeneous UV radiation field, we can use their results to interpret the effects of an anisotropic radiation field. The size of the halo is a sensitive function of the strength of the UV field. The weaker the strength of the UV field, the smaller the halo becomes (cf Fig. 7 in FP). It is found that the halo will be almost absent in case the UV field is attenuated with a factor $e^{-\tau}$ with $\tau=3.8$, leaving the core exposed. In the case of an anisotropic radiation field, we therefore would expect a larger halo in the direction of the UV field. Such a configuration is typical of the individual clouds in the L134 complex. The slices displayed in Figs. 19 and 20 clearly show a decrease in density and an increase in velocity dispersion in the direction of the UV field. In L] 34 and 1.1780 the lower density regions are about twice as extended on the UV side due to the lack of a strong UV field on the shadow sides of the clouds. This mechanism offers a natural explanation for the location of the dense regions in L] 83, 1.134 and 1.1780 in the NW corner of the clouds.

The infrared morphology of the clouds at 60 and 100 μm is such that they appear elongated in the direction of the radiation field with the densest regions on the shadow side. The absence of an halo causes a higher density contrast on the shadow side. Since the heating sources are situated behind the L134 complex (sect. 4.1), the shadow side with the ammonia cores are nearest to us, whereas the extended halo should be on the far end of the complex. Although the morphologic arc not as regularly defined as in the case of wind driven clouds, the CO and ^{13}CO (or 60 and 100 μm) images can be used to determine the direction of the radiation field acting upon clouds.

9. Conclusions

By analyzing CO, ^{13}CO , C^{18}O , infrared, and extinction data in a number of dark and translucent clouds in the L134 complex we have obtained the following results.

1. The nearby Upper Scorpius OB association and the star ζOph could enhance the UV radiation field by a factor 3 as high as 3 at 1000 \AA . The position of these sources is such that the field is illuminating the complex from one side.
2. For L134, L183, and L169 the correlation between ^{13}CO integrated emission and A_B yields a linear relationship. The ratios W_{13}/A_B are similar and the average value is not significantly different from other studies.
3. The ^{13}CO emission in the four densest clouds exhibits a good linear correlation with ΔI_{100} (defined in eq. [4]). This result implies that ΔI_{100} traces the same cloud regions as ^{13}CO . As a consequence, the regions of strong 60 μm emission delineate regions where the UV field is still present.
4. The density distribution in the four densest clouds as traced in A_B and I_{100} follow roughly exponential laws. The value of the exponent lies between 0.9 and 1.9.
5. The complex contains at least 18 ^{13}CO clumps. The clumps obey a size-linewidth relationship consistent with a powerlaw with exponent 0.5. The size-luminosity relationship follows closely a powerlaw with exponent 2.5. The ambient pressure acting upon the ^{13}CO clumps is of order $p/k = 2 \times 10^4 \text{ K cm}^{-3}$.
6. Slices through L134 and L1780 clearly show that the molecular and infrared emission are correlated with the anisotropy of the radiation field. The best tracer to determine the illuminated and shadow side of the cloud are W_{13}/W_{18} and $T_R(\text{CO})$: both drop towards the shadow side.
7. The isotropic UV radiation field affects the density distribution in the clouds. The densest regions - delineated by C^{18}O and the ammonia cores - are situated on the edges of the shadow sides of the clouds. The clouds are defined by the 100 μm , CO, and ^{13}CO morphologies.
8. We find a higher density contrast on the shadow side of the clouds which supports the view that lowering the strength of the UV field causes smaller halos around clouds.

Acknowledgements The research described in this paper was carried out by the Jet Propulsion Laboratory, California Institute of Technology, and was sponsored by the National Research Council and NATO through an agreement with the NASA. R.J.L. acknowledges partial support of a research associateship administered by the National Research Council. R.J.L. also acknowledges support from the University of Nagoya and able assistance from staff and students while carrying out the CO observations in the winter

of 1990/91. We are very grateful to K. Mattila and G. Schnur who kindly provided us the extinction data of the main complex, and to the IPAC staff for assistance in producing and understanding the infrared maps.

Table 1: Main Clouds analyzed in this study.

Cloud	R.A. (1950)	Dec. (1950)	Data used
L134	155100	-043000	IR, CO, ^{13}CO , C^{18}O , A_B
L169	154830	-033000	IR, CO, ^{13}CO , A_B
L183	155130	-023000	IR, CO, ^{13}CO , C^{18}O , A_B
L1780	153700	-070000	IR, CO, ^{13}CO , A_B
MBM 39	160300	+003000	IR, CO, ^{13}CO
MBM 38	155730	-013000	IR, CO, ^{13}CO

Table 2. Regression parameters for the 4 main clouds
 R : Correlation coefficient, **N** : Number of pixels/spectra involved

Cloud	Correlation between W_{13} and A_B				Correlation between I_{100} and A_B			
	W_{13}/A_B K km/s/m	Constant mag	R	N	I_{100}/A_B MJy/sr/mag	Constant mag	R	N
L183	1.3*0.3	0.4±0.2	0.82	293	2.1±0.6	-0.3±0.7	0.75	302
L134	1.4±0.2	0.4*0.3	0.87	143	2.9±0.3	-0.2±0.2	0.91	178
L169	1.3*0.5	0.6±0.6	0.67	198	3.7±0.7	+0.3±0.3	0.93	259
L1780	0.41±0.2	0.2±0.5	0.65	96	5.9*0.5	+0.0±0.1	0.92	151

Cloud	Correlation between ΔI_{100} and W_{13}				Correlation between ΔI_{100} and A_B			
	$\Delta I_{100}/W_{13}$ MJy/sr/ (Kkm/s)	constant Kkm/s	R	N	$\Delta I_{100}/A_B$ MJy/sr/mag	Constant mag	R	N
L183	1.3±0.2	0.6±0.4	0.88	306	1.6*0.3	0.1±0.4	0.82	316
L134	1.5*0.1	0.3*0.3	0.93	159	2.1±0.3	0.3±0.2	0.86	178
L169	1.5*0.3	0.1±0.5	0.82	197	1.7±0.4	0.6±0.4	0.77	259
L1780	5.3*0.4	-0.1*0.2	0.92	96	2.0±0.7	0.3*0.3	0.89	151

Table 3. Average Parameters for $A_B > 2$ mag

Cloud	N_{13}/W_{13} $10^{14} \text{ cm}^{-2}(\text{K km/s})^{-1}$	T_x K
L183	15 ± 1	16 ± 2
L134	13 ± 1	17 ± 3
L169	12 ± 1	14 ± 3
L1780	10 ± 1	9 ± 2

Table 4. Derived PowerLaw Density Distributions

Cloud	Tracer	
	A_B	I_{100}
L183	1.1 ± 0.2	0.9 ± 0.2
L134	1.9 ± 0.2	1.4 ± 0.2
L169	0.9 ± 0.2	1.2 ± 0.2
L1780	1.6 ± 0.2	1.1 ± 0.2

Table 5a. Measured Properties of Clumps

Ident.	R.A. (1950)	Dec. (1950)	R pc	T_{ex} K	AV km/s	V_{ls} km/s	L_1 Kkm/s pc ²
L1780	15 36 56	-07 02	0.16	11.2	0.55	3.80	0.10
L183a	15 51 42	-03 14	0.32	15.4	0.97	2.0%	0.65
L183b	15 51 26	-02 50	0.50	13.4	1.23	2.74	2.45
L183c	15 50 24	-03 25	0.16	10.8	0.73	2.99	0.13
L183d	15 52 52	-02 58	0.12	12.6	0.49	2.51	0.06
L183e	15 49 58	-03 05	0.29	15.4	1.14	2.25	0.47
L183f	15 48 38	-03 23	0.27	13.6	1.21	3.65	0.50
L183g	15 49 57	-03 37	0.17	12.9	0.58	1.94	0.13
L183h	15 49 21	-03 29	0.35	13.7	0.81	2.60	0.69
L183i	15 48 04	-03 56	0.09	11.7	0.48	2.52	0.03
L134a	15 51 36	-04 34	0.12	18.0	0.56	1.13	0.04
L134b	15 51 00	-04 36	0.48	14.5	1.04	2.49	2.26
L134c	15 50 24	-05 00	0.05	11.1	0.38	2.60	0.01
MBM39a	16 02 59	+00 33	0.10	11.7	0.58	2.34	0.04
MBM39b	16 03 29	+00 27	0.08	10.4	0.57	2.86	0.02
MBM38a	15 57 47	-01 19	0.09	9.7	0.58	0.86	0.02
MBM38b	15 57 18	-01 32	0.19	12.8	0.54	1.12	0.11
MBM38c	15 56 35	-01 37	0.08	10.2	0.38	1.80	0.02

Table 5b. Derived Parameters of Clumps

ident	σ_{thermal} km/s	σ_{turb} km/s	σ_{gas} km/s	$\log(M_{13})$ M_{\odot}	$\log(n)$ 10^3 cm^{-3}	$\log(E_{\text{gr}})$ 10^{43} erg	$\log(E_{\text{turb}})$ 10^{43} erg	p/k 10^4 K cm^{-3}
L1780	0.06	0.24	0.74	-0.01	-0.01	-1.3	-0.5	1.3
L183a	0.07	0.43	1.16	0.80	-0.10	0.0	0.8	3.2
L183b	0.06	0.55	1.40	1.37	-0.13	1.0	1.6	4.4
L183c	0.06	0.32	0.89	0.08	0.07	-1.1	-0.2	2.8
L183d	0.06	0.21	0.70	-0.21	0.16	-1.6	-0.8	1.5
L183e	0.07	0.51	1.32	0.66	-0.12	-0.2	0.8	4.6
L183f	0.06	0.54	1.37	0.68	0.00	-0.1	0.9	6.7
L183g	0.06	0.25	0.78	0.10	0.01	-1.1	-0.4	1.4
L183h	0.06	0.36	0.99	0.82	-0.18	0.0	0.7	1.7
L183i	0.06	0.21	0.68	-0.53	0.17	-2.1	-1.1	1.5
L134a	0.07	0.24	0.83	-0.37	0.00	-1.9	-0.8	1.5
L134b	0.06	0.47	1.22	1.34	-0.10	0.9	1.4	3.0
L134c	0.06	0.16	0.60	-1.19	0.23	-3.2	-2.0	1.2
MBM39a	0.06	0.26	0.77	-0.45	0.20	-2.0	-0.9	2.5
MBM39b	0.05	0.25	0.75	-0.74	0.22	-2.4	-1.2	2.6
MBM38a	0.05	0.25	0.74	-0.68	0.02	-2.4	-1.1	1.7
MBM38b	0.06	0.23	0.75	0.02	-0.18	-1.3	-0.5	0.8
MBM38c	0.05	0.16	0.59	-0.77	0.19	-2.5	-1.6	1.0

References

- Abergel, A., Boulanger F., Mizuno, A., Fukui, Y. 1993, *ApJ(Letters)* in press
- Bachiller, R., Cernicharo, J. 1986, *A&A* 166, 283
- Benson, P.J., Myers, P.C. 1989, *ApJS* 71, 89
- Blaauw, A. 1991, in *The Physics of Star Formation and Early Stellar Evolution*, Eds. C.J. Lada, N.D. Kylafis, (Dordrecht: Kluwer), p125
- Bohlin, R. C., Savage, B. D., Drake J.F. 1978, *ApJ* 224, 132
- Boulanger, F., Falgarone, E., G., Puget, J. L., Helou, G. 1990, *ApJ* 364, 136
- Carr, J.S. 1987, *ApJ* 323, 170
- Casoli, F., Combes, F., Gerin, M. 1984, *A&A* 113, 99
- Chlewicki, G., Laureijs, R.J. 1988, *A&A* 207, L11
- Clark, F.O., Johnson, D.R. *ApJ* 247, 104
- Coulomb, F.R., Pöppel, W.G.L., Heiles, C. 1980, *A&AS* 40, 47
- Crane, F., Hegyi, D.J., Lambert D.L. 1991, *ApJ* 378, 181
- Crawford, D. L., Mandwewala, N. 1976, *PASP* 88, 917
- de Geus, E. J., de Zeeuw, P. T., Lub, J. 1989, *A&A* 216, 44
- de Geus, E. J., Bronfman, L., Thaddeus, P. 1990, *A&A* 231, 137
- Désert, F.X., Boulanger, F., Puget, J.L. 1990, *A&A* 237, 215
- Dickman, R.L. 1978, *ApJS* 37, 407
- Dickman, R. L., Herbst, W. 1990, *ApJ* 357, 531
- Draine, B.T., Anderson, 1985, *ApJ* 292, 494
- Draine, B.T. 1990, in *The Interstellar Medium in Galaxies* Eds. H.A. Thronson, Jr. and J.M. Shull, (Dordrecht: Kluwer)
- Falgarone, E., Puget, J.L. 1985, *A&A* 142, 157
- Franco, G.P. 1989, *A&A* 223, 313
- Glassgold, A. E., Huggins, P.J., Langer, W.I). 1985, *ApJ* 290, 615
- Good, J. 1988, WAC Internal Report
- Habing, H.J. 1968, *B.A.N.* 19, 421
- HcIou, G. 1989, in *Interstellar Dust*, IAU Symp. 135, Eds L.J. Allamandola, A.G.G.M. Tielens, p285
- Hildebrand, R.H. 1983, *QJRAS* 24, 267
- Kawabata, H., Fukui, Y., Takano, T., Fujimoto, Y., Kawabe, R., Sugitani, K., Takaba, H. 1985, *A&A* 151, 1
- Keto, E. R., Myers, P.C. 1986, *ApJ* 304, 466
- Kutner, M. L., Ulich, B. I. 1981, *ApJ* 250, 341
- Langer, W.D., Wilson, R.W., Goldsmith, P.F., Beichman, C.A. 1989, *ApJ* 337, 355
- Laureijs, R.J., Clark, F. O., Chlewicki, G., Wesselius, P.R. 1989, *A&A* 220, 226
- Laureijs, R.J., Clark, F. O., Prusti, T. 1991, *ApJ* 372, 185
- Leung, C. M., Kutner, M.L., Mead, K.N. 1982, 262, 583
- Loren, R.B. 1989a, *ApJ* 338, 925
- Loren, R.B. 1989b, *ApJ* 338, 925
- Lynds, B.T. 1962, *ApJS* 64, 1
- Magnani, L., Blitz, L., Mundy, L. 1983, *ApJ* 295, 402
- Malony, P. 1990, *ApJ*, 348, 1.9
- Mathis, J. S., Mezger, P.G., Panagia, N. 1983, *A&A* 128, 212
- Mathis, J. S., Whiffen, G. 1989, *ApJ* 341, 808
- Mattila, K. 1979, *A&A* 78, 253
- Mattila, K. 1986, *A&A* 160, 157

- Mattila, K., Schnur, G. 1995, in preparation
- Myers, P.C. 1983, *ApJ* **270**, 105
- Myers, P. C., Benson, P. 1983, *ApJ* **266**, 309
- Nozawa, S., Mizuno, A., Teshima, Y., Ogawa, H., Fukui, Y. 1991, *ApJS* **77**, 647
- Ogawa H., Mizuno, A., Hoko, H., Ishikawa, H., Fukui, Y. 1990, *Int. J. of IR and mm Waves* **11**, 717
- Oken, C. Gautier, N, Wheelock, S. 1988, IPAC Internal Report
- Savage, B. D., Ma(his, J.S. 1979, *ARA&A* **17**, 73
- Schloerb, F.P., Loren, R.B. 1981, *Symp. on the Orion Nebula to Honor H. Draper*, Eds. A.E. Glassgold, P.J. Huggins & E.L. Schucking, Ann. NY Ac. of Sci. 395, 32
- Scoville, N. Z., Good, J.C. 1989, *ApJ* **339**, 149
- Solomon, P.M., Rivolo, A.R., Barrel, J.W., Yahil, A.M. 1987, *ApJ* **319**, 730
- Snell, R.L. 1981, *ApJS* **45**, 127
- Swade, D.A. 1989a, *ApJS* **71**, 219
- Swade, D.A. 1989b, *ApJ* **345**, 828
- Ungerechts, H., Walmsley, C. M., Winnewisser, G. 1983, *A&A* **88**, 259
- van Dishoeck, E. F., Black, J.H. 1988, *ApJ* **334**, 771
- Wheelock, S., Kester, D. 1989, IPAC Internal Repel-[
- Young, J. S., Goldsmith, P. F., Langer, W. D., Wilson, R.W., Carlson, E.R. 1982, *ApJ* **261**, 531
-

Figure Captions

Figure 1

The infrared sky around the L134 complex of clouds::

- a. Large scale map of the 100 μm infrared sky in galactic coordinates. A cylindrical projection has been used with projection center on $l=0^\circ, b=0^\circ$. The effective resolution is 0.5° . The dark clouds L134 and L183 are situated around $(l, b)=(2^\circ, 34^\circ)$. The bright region at $l=350^\circ, b=15^\circ$ is the Ophiuchus region. Contours at 10, 15, 20, 40, and 100, 200, . . . 6400 MJy/sr. The white box marks approximately the region covered by Fig. 2b.
- b. The vicinity of the L134 complex at 100 μm in galactic coordinates. Contours at 3.5, 7, . . . 35 MJy/sr. From Table 1, the clouds MBM38, MBM39, L1780, and L134 are indicated, the remaining clouds listed in Table 1 are labeled in Fig. 2.

Figure 2

Images in the IRAS wavelength bands of the main complex containing the dark clouds L183, L169, and L134. The 12, 25, 60, and 100 μm images are displayed in the upper left, upper right, lower left, and lower right panel, respectively. The clouds are labeled in the 100 μm image. The spatial resolution in the maps is $5'$. The following contours have been plotted: 12 μm : intervals of 0.1 MJy/sr, highest contour at 1.1 MJy/sr; 25 μm : intervals of 0.1 MJy/sr, highest contour at 1.1 MJy/sr; 60 μm : 0.4 MJy/sr, highest contour at 4.0 MJy/sr; 100 μm : 2 MJy/sr, highest contour at 22 MJy/sr.

Figure 3

Same as Fig. 2. The infrared images of L1780. Contours: 12 μm : intervals of 0.15 MJy/sr, highest contour at 1.5 MJy/sr; 25 μm : intervals of 0.2 MJy/sr, highest contour at 1.4 MJy/sr; 60 μm : 0.5 MJy/sr, highest contour at 5.0 MJy/sr; 100 μm : contours at 1.0, 2.0, 4.5, 7.0, . . . 22.0 MJy/sr.

Figure 4

Same as Fig. 2. MBM 39 is detected only at 60 and 100 μm , Contours: 60 μm : intervals of 0.3 MJy/sr, highest contour at 2.1 MJy/sr; 100 μm : 1.5 MJy/sr intervals, highest contour at 15 MJy/sr.

Figure 5

Same as Fig. 2. The infrared images of MJ3M 38. Contours: 12 μm : intervals of 0.1 MJy/sr, highest contour: 1.0 MJy/sr; 25 μm : same as at 12 μm ; 60 μm : intervals of 0.3 MJy/sr, highest contour at 1.8 MJy/sr; 100 μm : 1 MJy/sr, highest contour at 10 MJy/sr.

Figure 6

The $\text{CO}(J=1-0)$ channel maps of $T_A^* \Delta v$ of the central region in the complex. Each map covers a velocity interval of $\Delta v = 0.4 \text{ km/s}$. The center velocity in km/s is indicated in the upper right corners of the maps. Each dot marks an observation and the grid spacing is $3'$. The nominal resolution of the telescope is $2.6''$. The maps have been smoothed with a gaussian of 2.5 FWHM . The large crosses mark the position and velocity of the ammonia cores obtained by Myers & Benson (1989) for L134, and by Ungerechts et al. (1983) for L183. The contours are in steps of 1 K km/s , the lowest contour is 0.75 K km/s .

Figure 7

Similar to Fig. 6 but for $^{13}\text{CO}(J=1-0)$. The contours are in steps of 0.3 K km/s , lowest contour is at 0.2 K km/s .

Figure 8

The velocity integrated emission in the complex for CO and ^{13}CO , the integration interval runs from 0 to 5 km/s. The maps have been smoothed to an effective resolution of 5' FWHM. The crosses mark the positions of the ammonia cores. In the CO map the contours are in steps of 4 Kkm/s, the lowest contour is at 3 Kkm/s. In the ^{13}CO map the contours are in steps of 0.75 Kkm/s, the lowest contour is at 0.5 Kkm/s.

Figure 9

The velocity integrated maps for L1780, the integration intervals are 2.3 to 4.7 km/s for CO and 2.9 to 4.7 km/s for ^{13}CO . The maps have been smoothed with a gaussian of 2.5 arcmin FWHM. The CO contours are given in steps of 1 Kkm/s, the lowest contour is at 1 Kkm/s; ^{13}CO contours are in steps of 0.3 Kkm/s, the lowest contour is at 0.2 Kkm/s.

Figure 10

Similar as Fig. 9, but for MBM 39. Integration intervals from 1.2 to 3.6 km/s for CO and 1.6 to 3.6 km/s for ^{13}CO . The CO contours are given in steps of 1 Kkm/s, the lowest contour is at 1.5 Kkm/s; ^{13}CO contours are in steps of 0.25 Kkm/s, the lowest contour is at 0.25 Kkm/s.

Figure 11

Similar as Fig. 9, but for MBM 38. Integration intervals from -0.8 to 2.8 km/s for CO and 0 to 2 km/s for ^{13}CO . The CO contours are given in steps of 1 Kkm/s, the lowest contour is at 1.5 Kkm/s; ^{13}CO contours are in steps of 0.3 Kkm/s, the lowest contour is at 0.35 Kkm/s.

Figure 12

The pixel-to-pixel correlation diagrams of W_{13} versus A_B for the four main clouds in the complex. The derived regression parameters are listed in Table 2.

Figure 13

The ratio N_{13}/W_{13} as a function of blue extinction. The derived parameters are listed in Table 2.

Figure 14

The correlation between I_{100} and A_B . The derived regression parameters are listed in Table 2.

Figure 15

The maps of ΔI_{100} obtained by applying eqn. 4. For all clouds we have used $\Theta=0.21$ except for L1780 where $\Theta=0.27$. a. The main complex, contour intervals of 1.5 MJy/sr, highest contour is 1.5 MJy/sr. b. L1780, contour intervals of 1 MJy/sr, highest contour is 11 MJy/sr. c. MBM 39, contour intervals of 0.75 MJy/sr, highest contour at 4.5 MJy/sr. d. MBM 38, contour intervals of 0.5 MJy/sr, highest contour at 3.5 MJy/sr.

Figure 16

Pixel to pixel correlation diagrams of ΔI_{100} and W_{13} . The derived regression parameters are listed in Table 2.

Figure 17

Determination of the global density distribution in L183. Plotted is the distribution of the number of pixels over the surface of the cloud with values less than a given A_B , I_{100} or W_{13} value. The distributions have been normalized by the total amount of pixels (which is equivalent to the total area) of the cloud and the upper 10 percentile point. The 2 dashed lines are the predicted relationships

assuming spherical symmetry and $r^{-1.1}$ and r^{-2} power law density distributions. The parameters for the other clouds are listed in Table 3.

Figure 18

The ratio W_{13}/W_{18} as a function of A_B as observed L183 and L134. The ordinate on the right hand side denotes the value for R_N , the normalized abundance ratio as defined in eqn. 7.

Figure 19

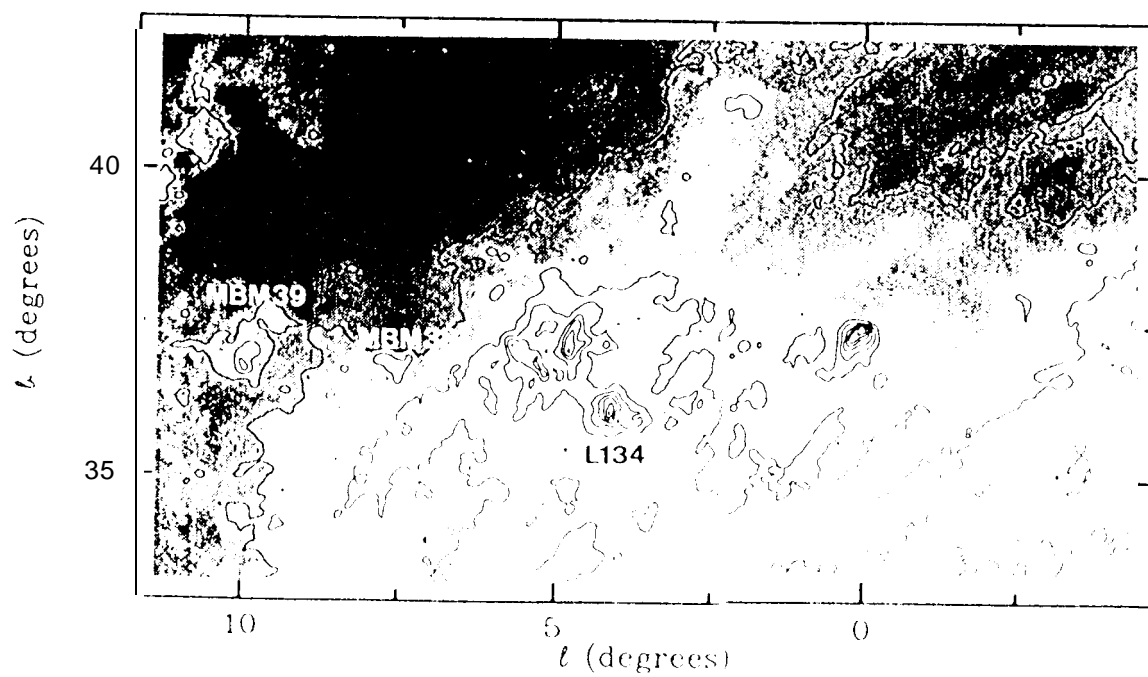
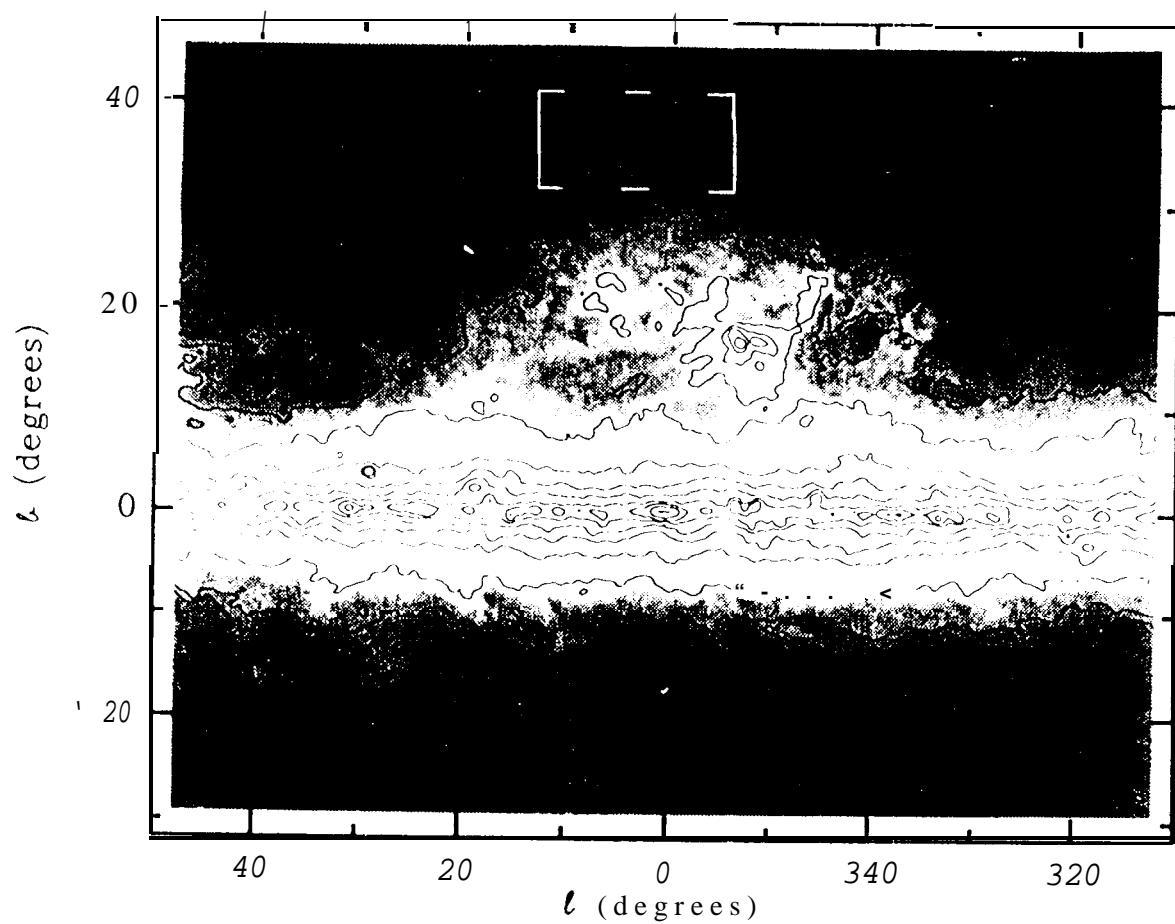
The variation of different tracers in L134 along a line parallel 10 (the assumed direction of the ambient UV field). Position O corresponds to RA 15^h51^m00^s, Dec -4°30'00" which is close to the position of the ammonia core in the cloud. The position angle of the slice is 335°. The tracers are I_{12} and I_{25} (panel a), I_{60} and I_{100} (panel b), integrated line emission for different CO isotopes (panel c), CO peak temperature (d), extinction and I_{100} (panel e), the infrared colors (panel f), measures for infrared emissivity (panel g) and the ratio of integrated line emission of ^{13}CO and C^{18}O (panel h). Note that in L134 the extinction A_B at position (0,0) is a lower limit, therefore the derived parameters in (0,0) are also limits.

Figure 20

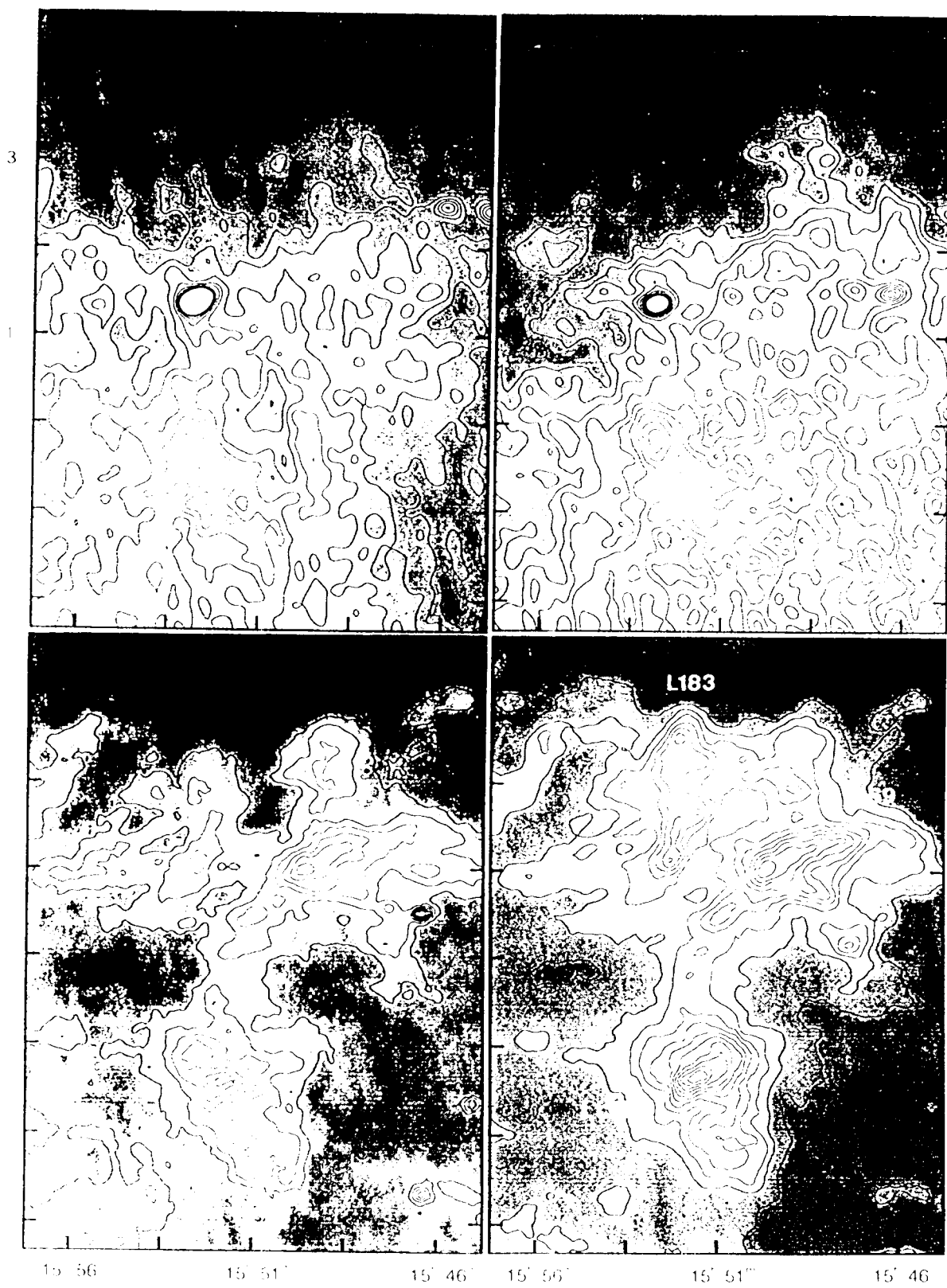
Similar as Fig. 19: slice through L1780.

Figure 21

- a. The size versus ^{13}CO luminosity relationship for 18 ^{13}CO clumps in the complex.
- b. The size versus linewidth relationship for the ^{13}CO clumps in the complex.



Declination 950'



Right Ascension (1950)

Fig 2

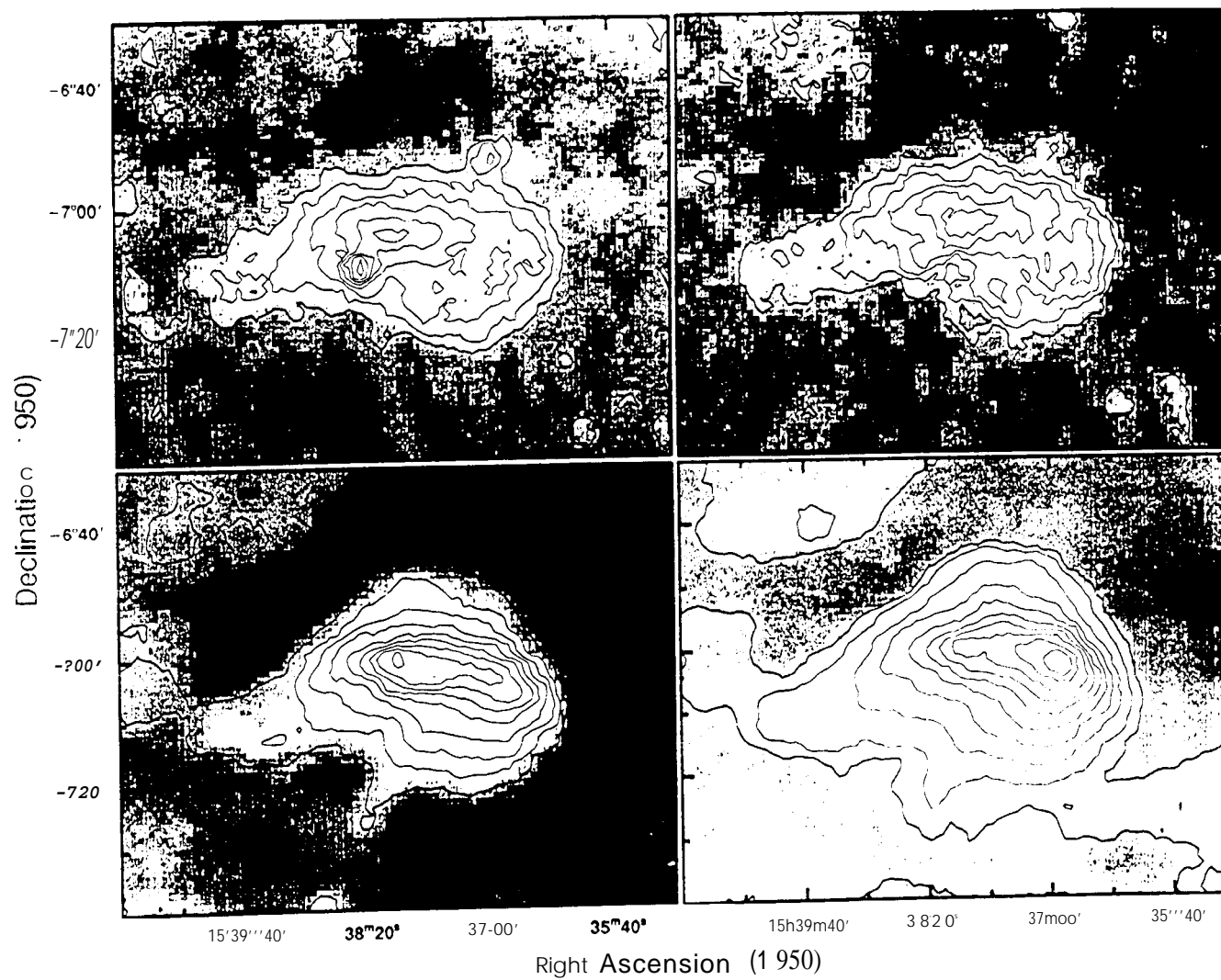


Fig 3

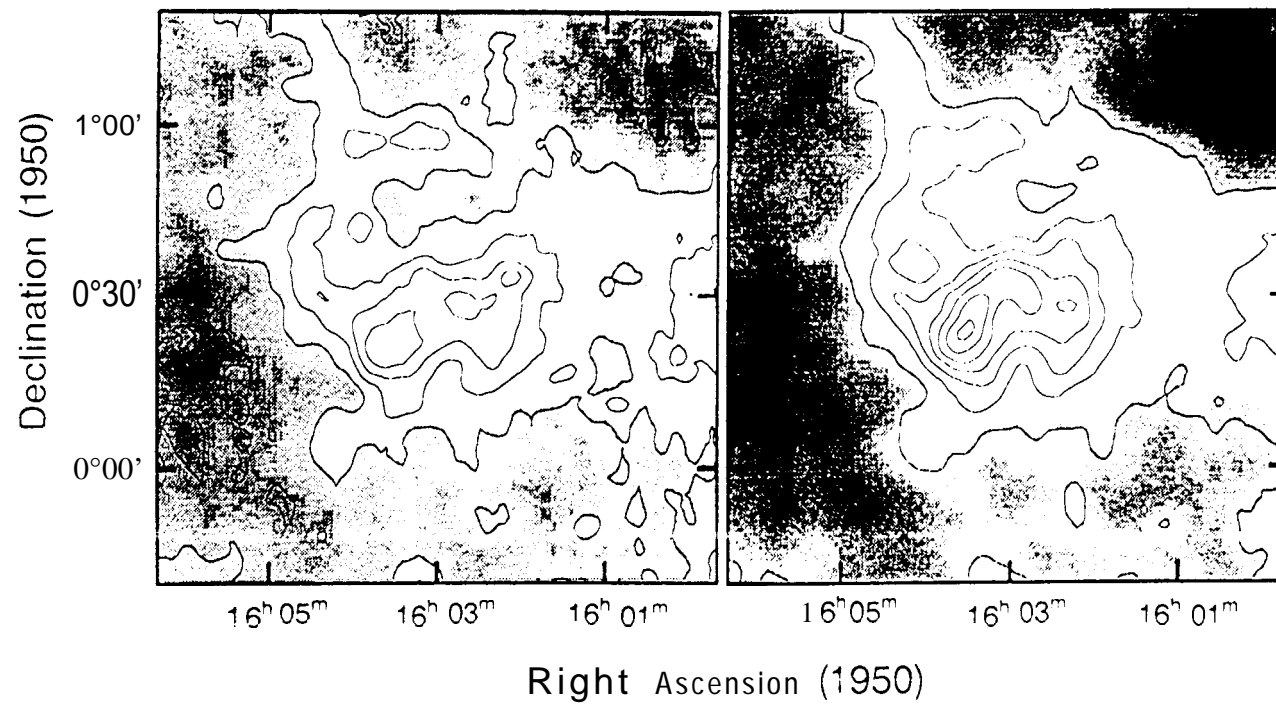


Fig 4

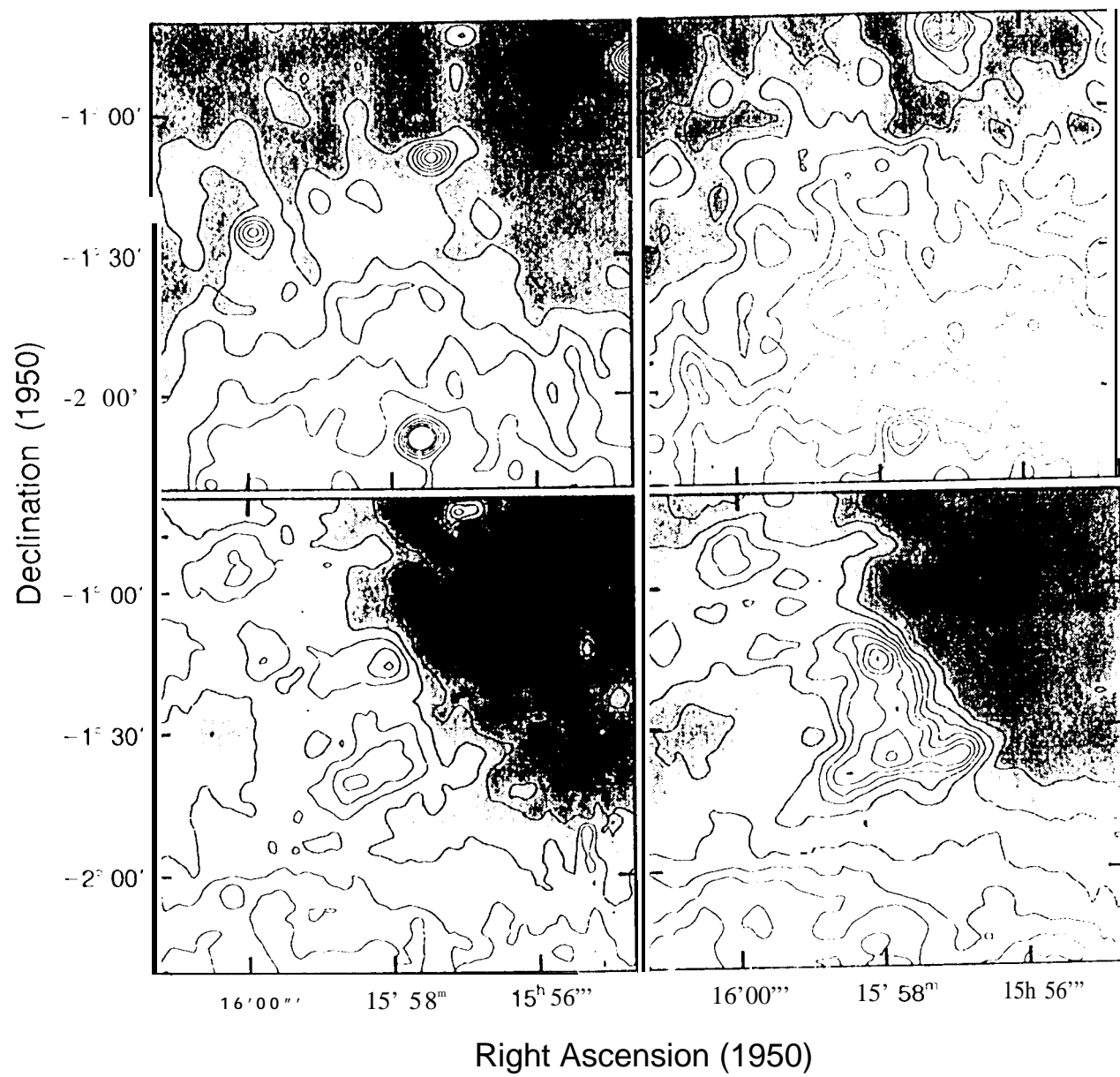


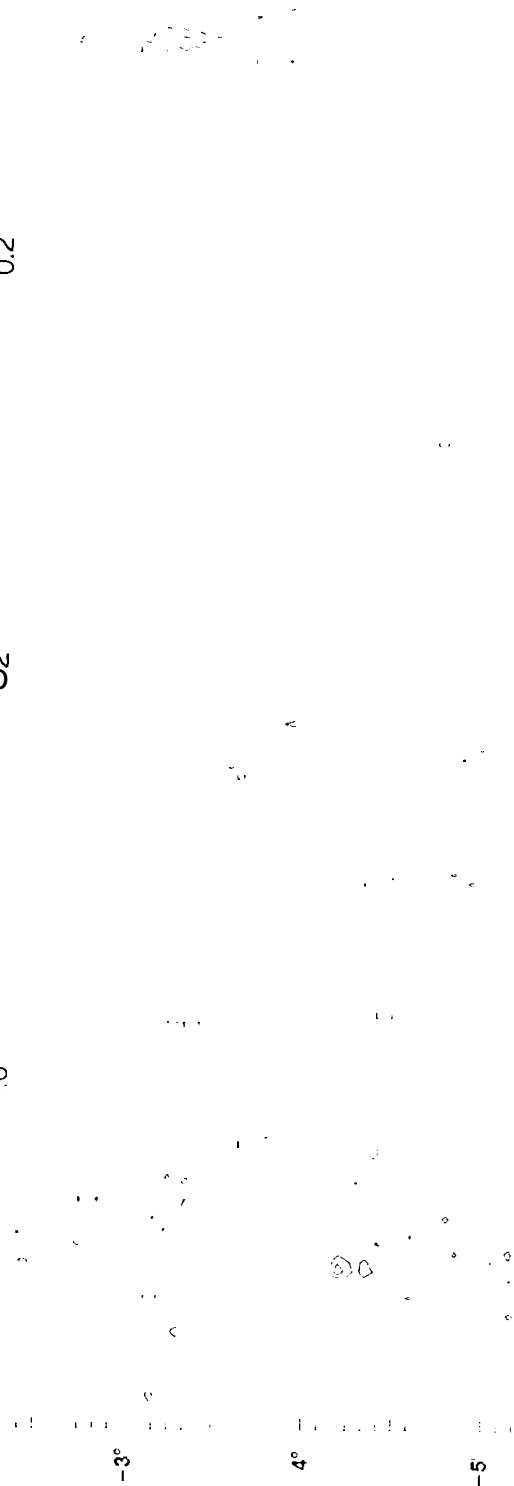
Fig 5

0.6

0.2

0.2

0.6



2.2

8

4

10



48m

50m

52m

15h 54m

48m

50m

52m

15h 54m

48m

50m

52m

15h 54m

48m

50m

52m

15h 54m

48m

50m

52m

Right Ascension (1950)

Fig 6

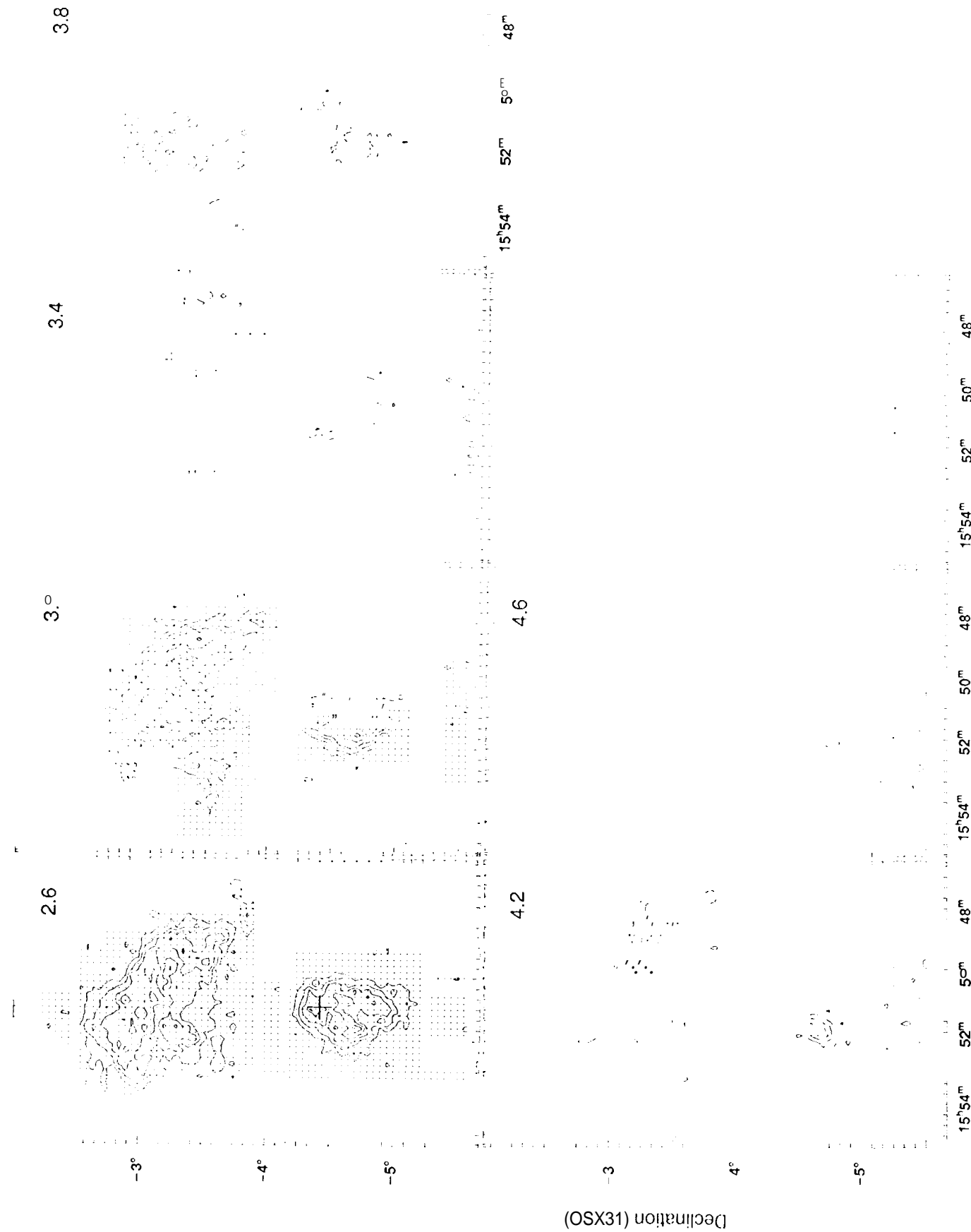


Fig. 6. (continued)



Fig 7

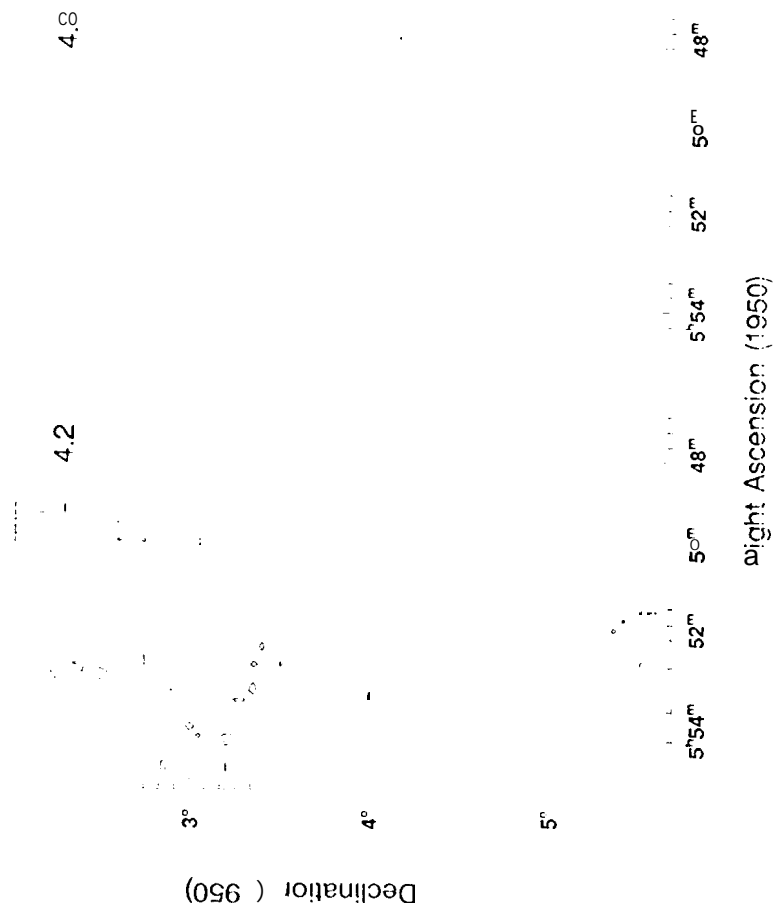
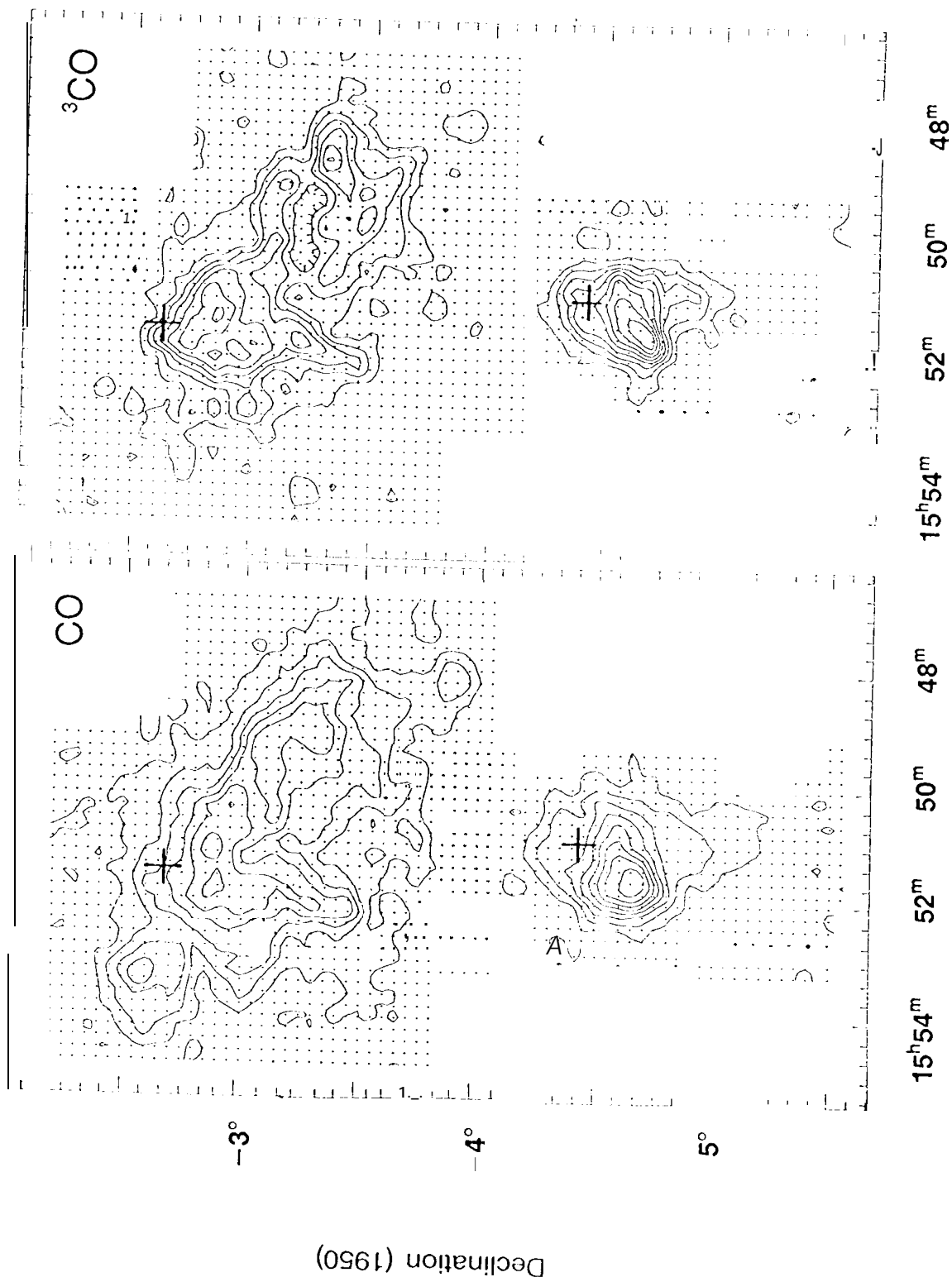


Fig 7 : continued)



Right Ascension (1950)

Fig 8.

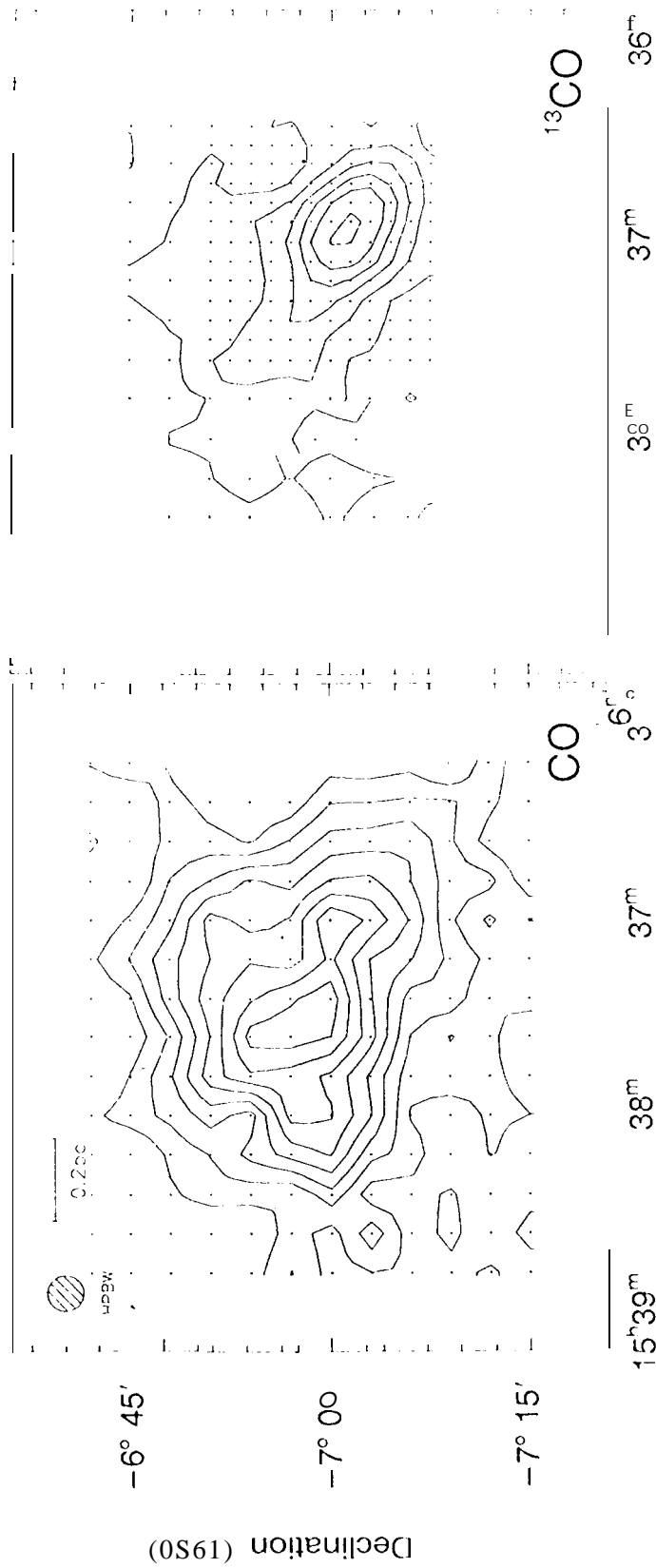


Fig. 9

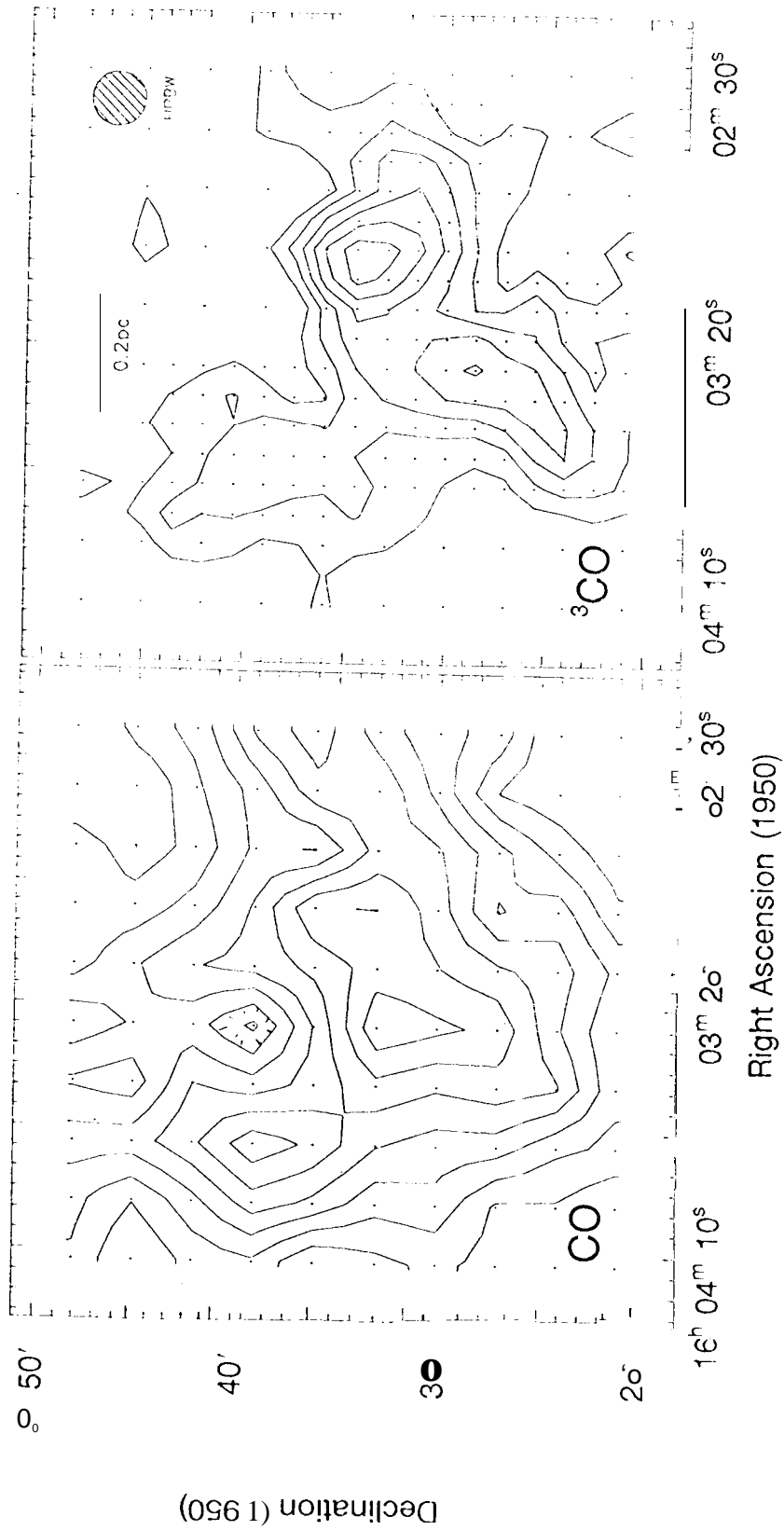


Fig 10

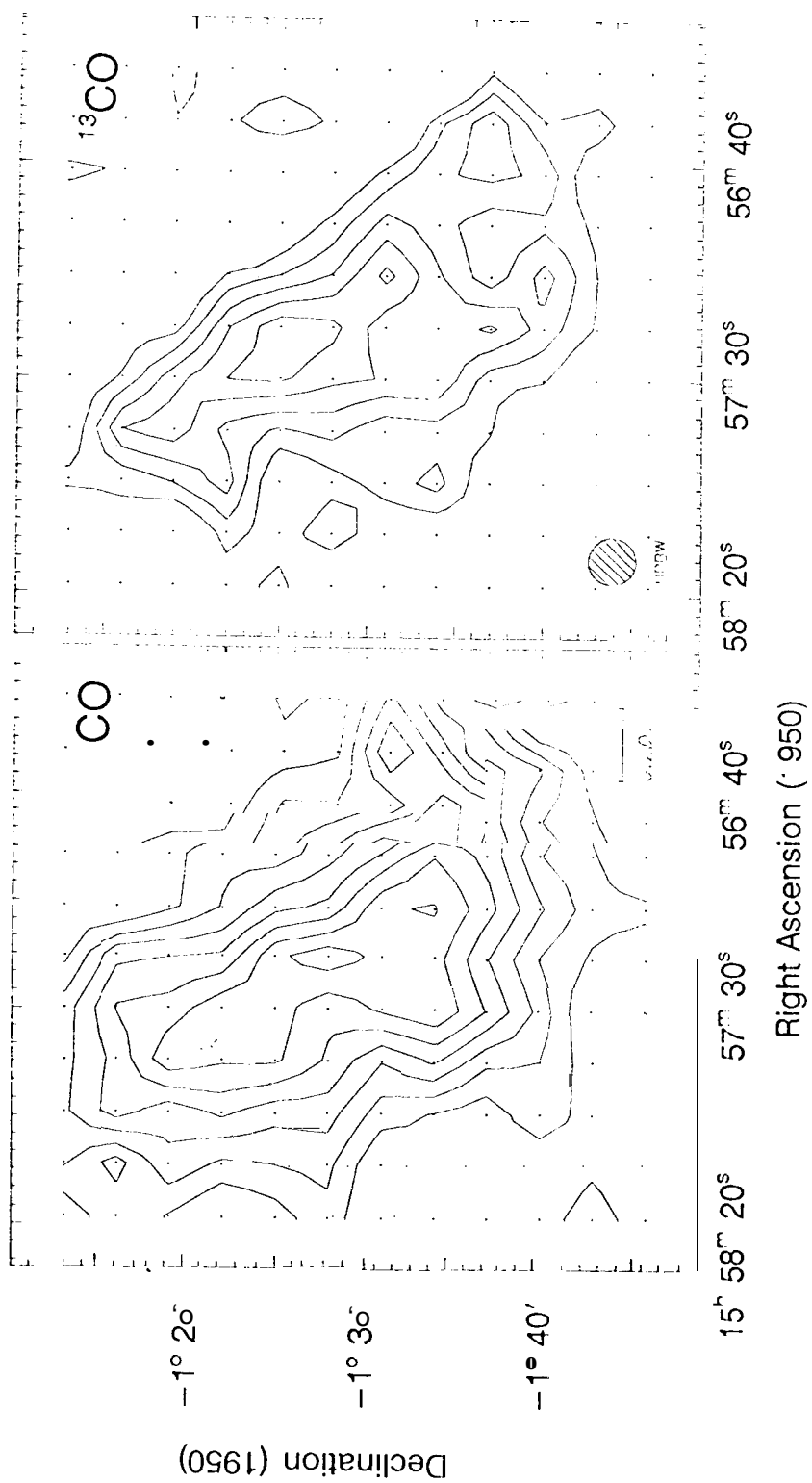


Fig 11

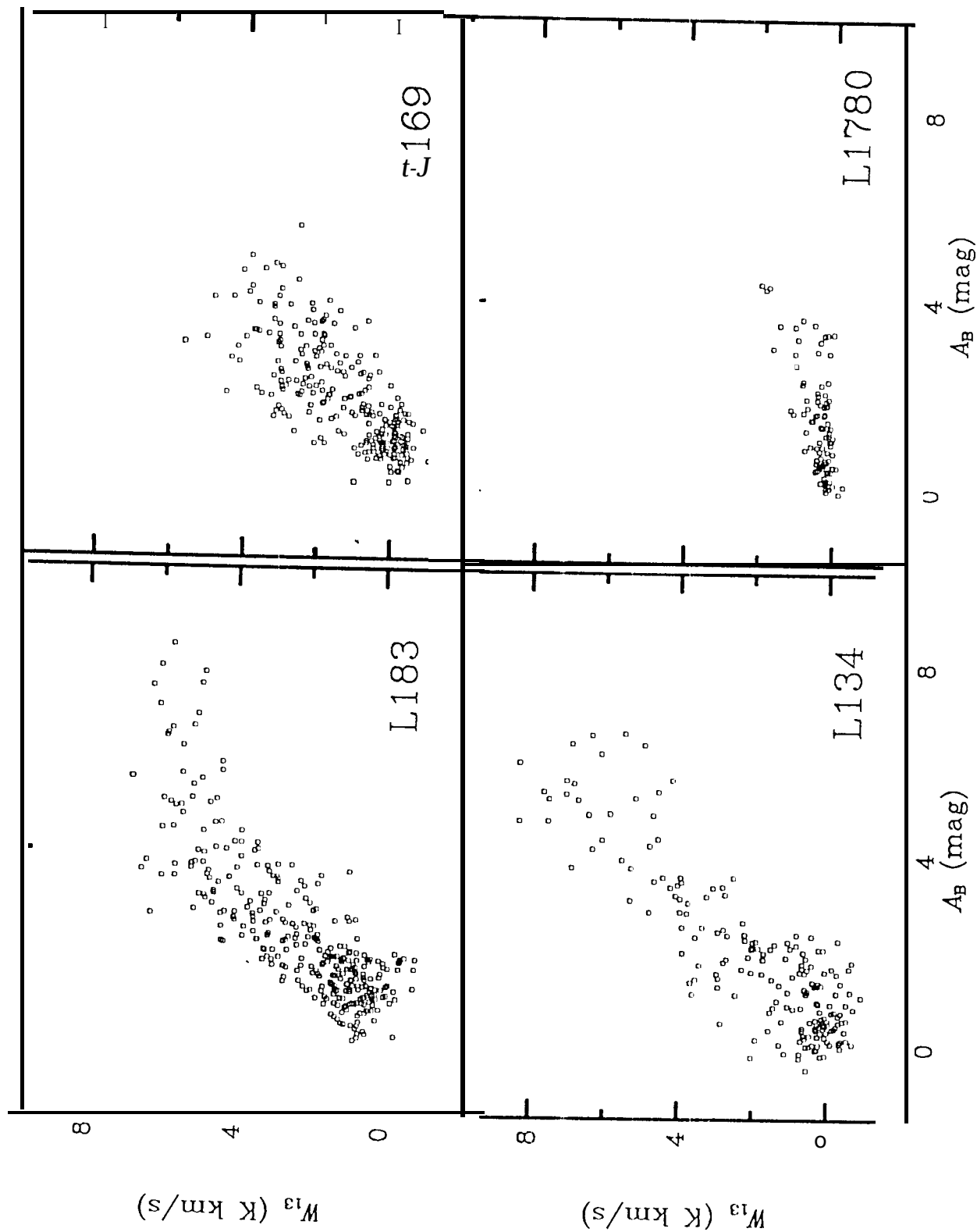


Fig 12

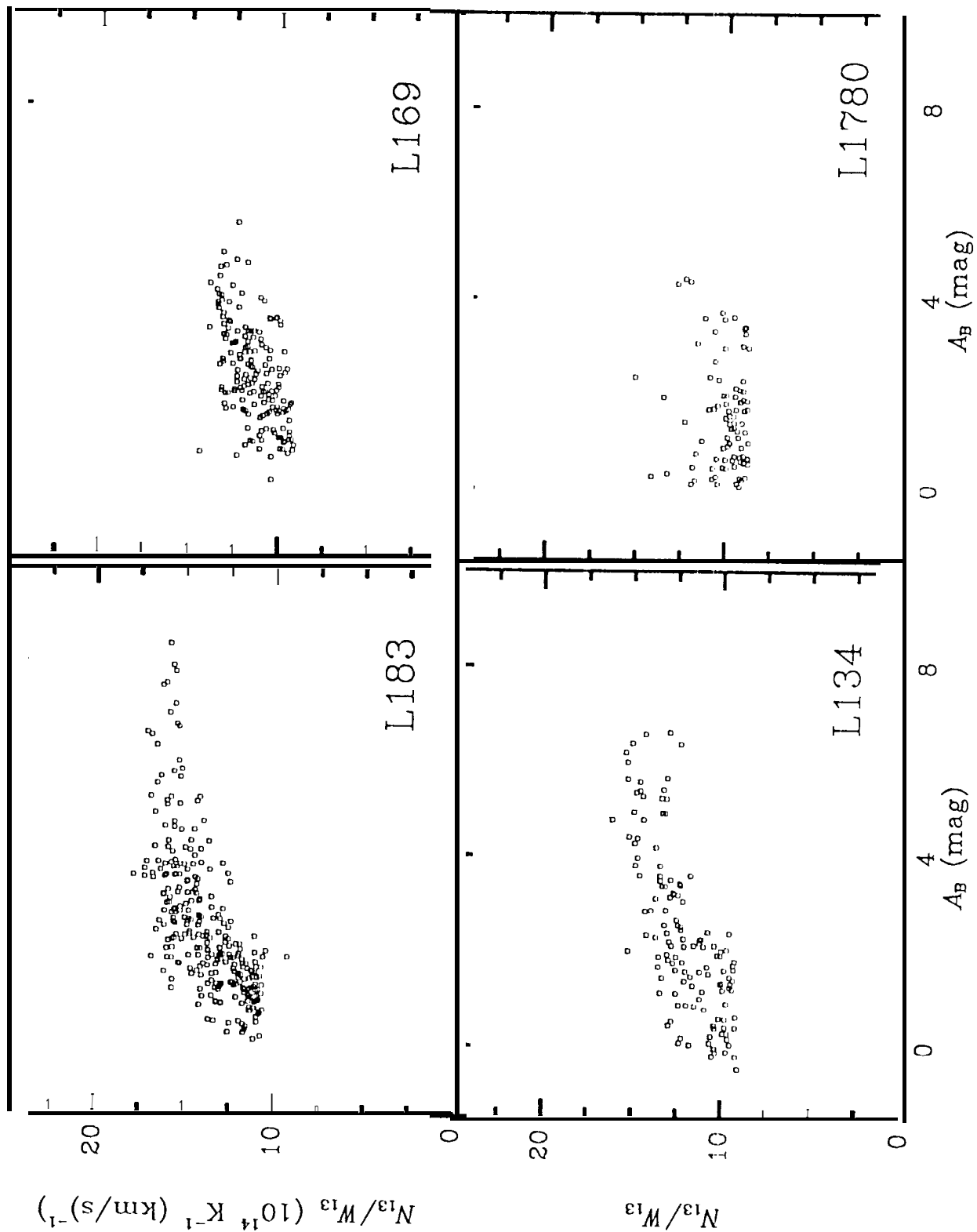
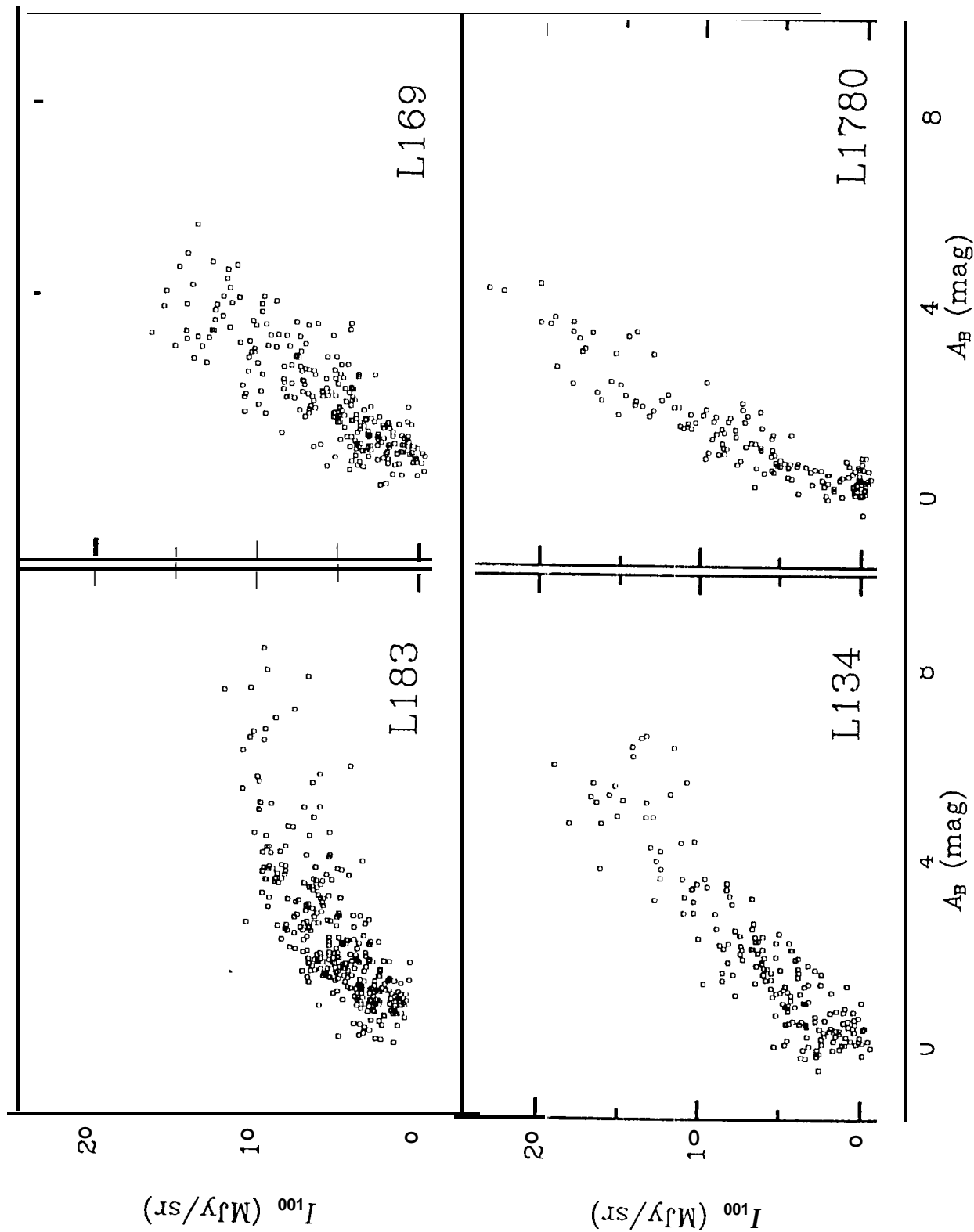


Fig 13



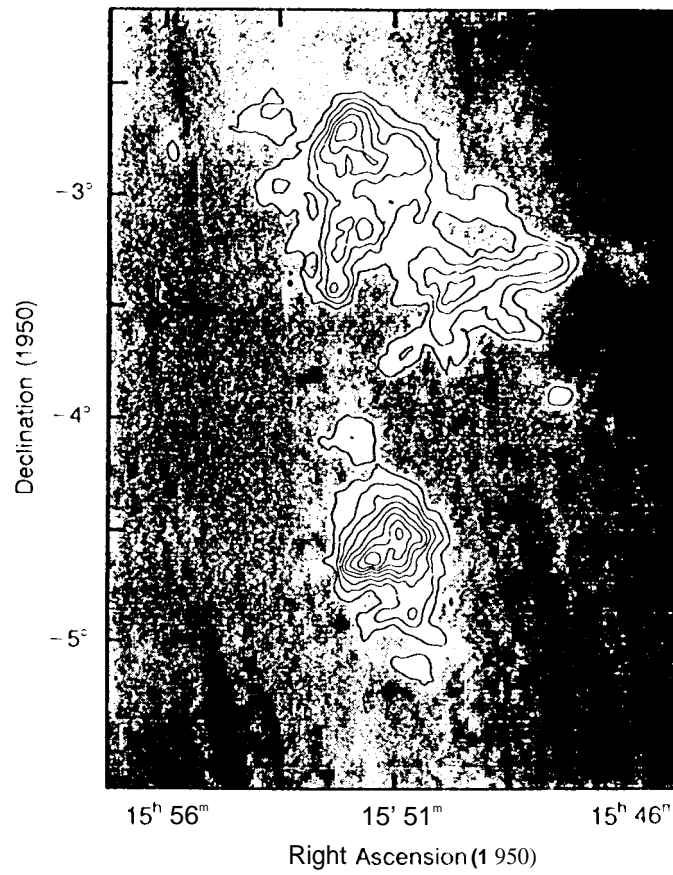


Fig 15a

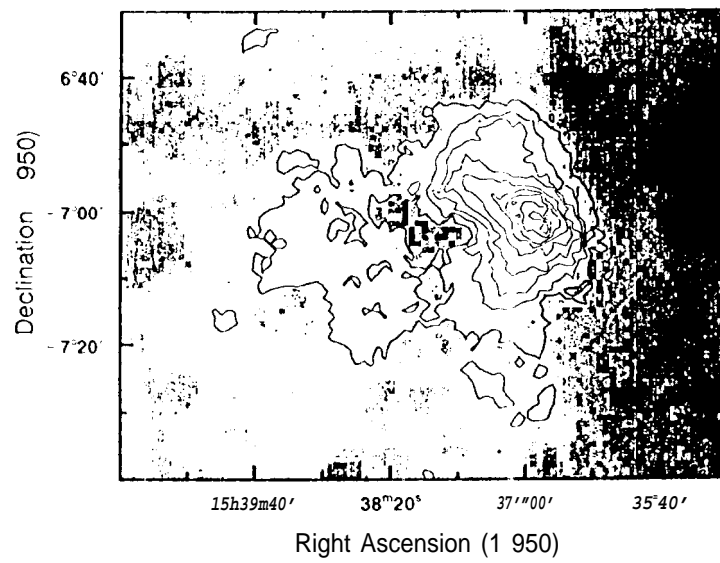


Fig 15 b

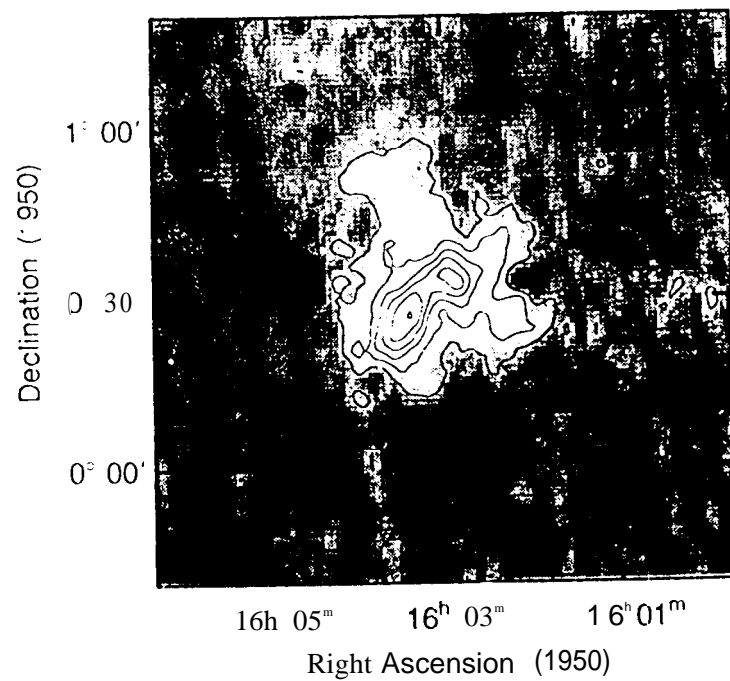


Fig 15 c

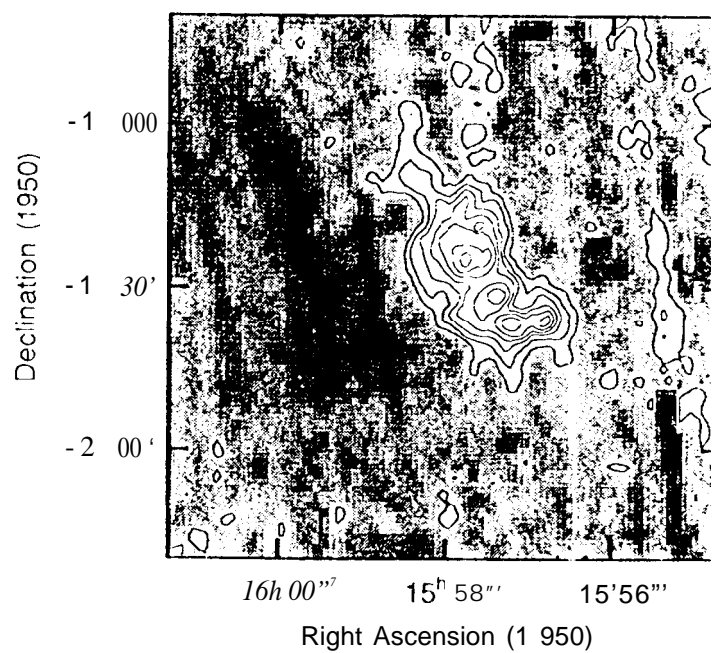


Fig 15 d

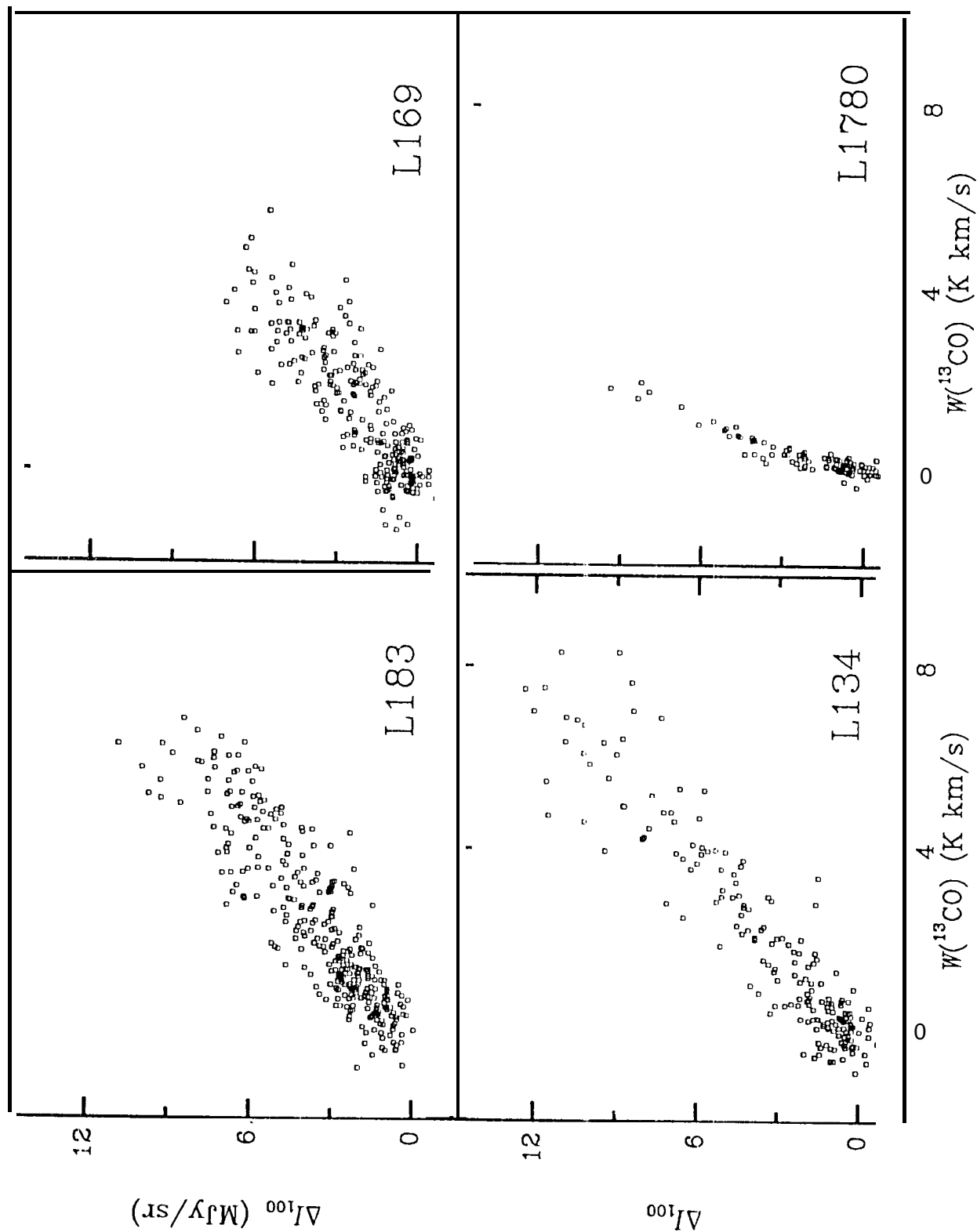


Fig 1

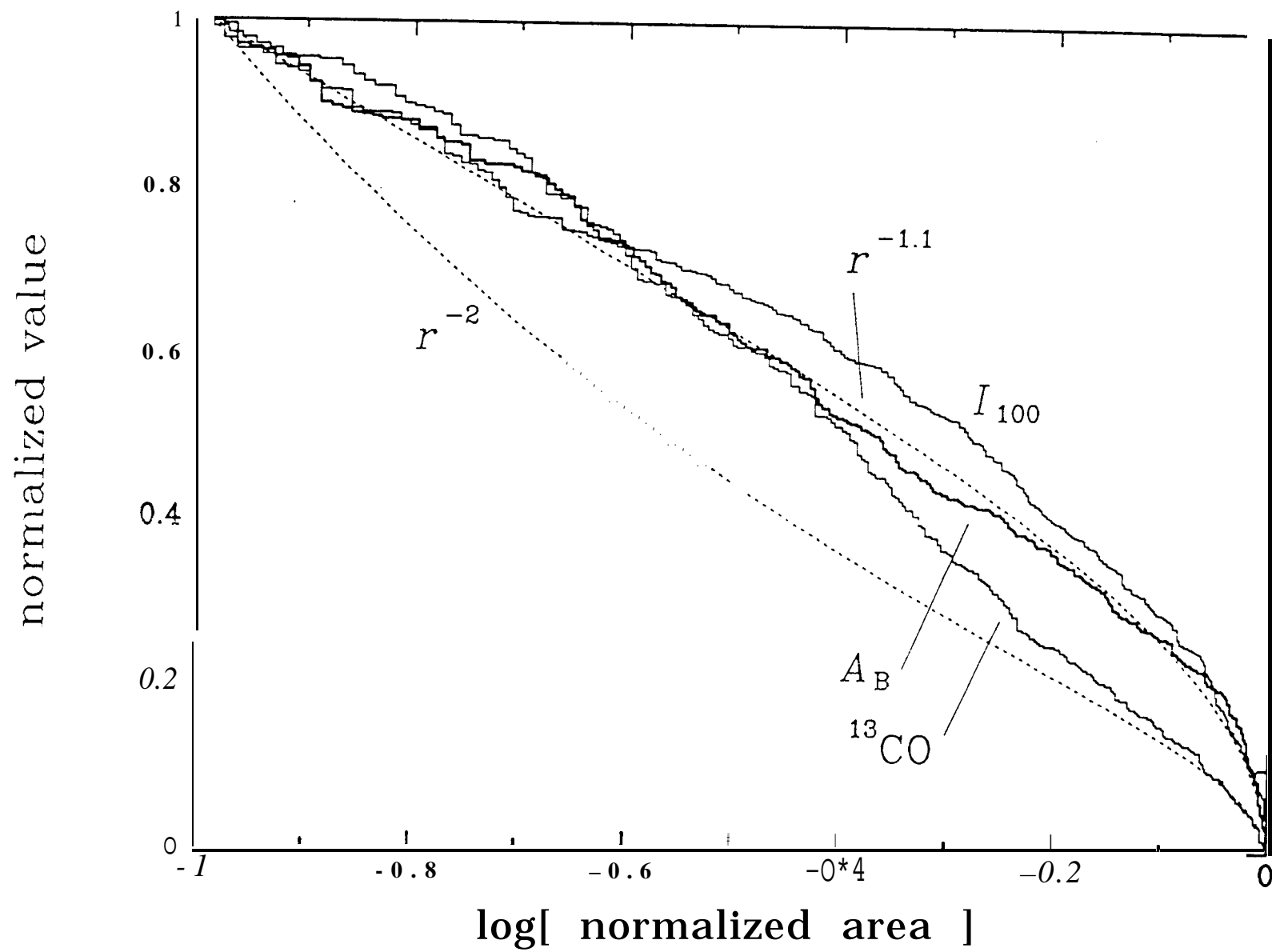


Fig 17

